

PARTICLE DISPERSION WITHIN ZONAL JETS
IN TWO-LAYER BETA-PLANE TURBULENCE

A Thesis

by

JENNIFER CLAIRE ROMAN

Submitted to the Office of Graduate Studies of
Texas A&M University
in partial fulfillment of the requirements for the degree of
MASTER OF SCIENCE

August 1996

Major Subject: Meteorology

PARTICLE DISPERSION WITHIN ZONAL JETS
IN TWO-LAYER BETA-PLANE TURBULENCE

A Thesis

by

JENNIFER CLAIRE ROMAN

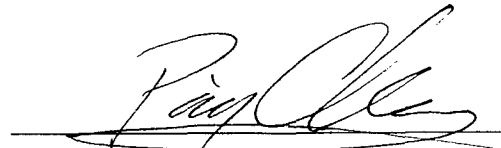
Submitted to Texas A&M University
in partial fulfillment of the requirements
for the degree of

MASTER OF SCIENCE

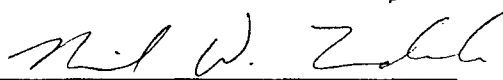
Approved as to style and content by:



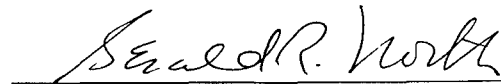
R. Lee Panetta
(Chair of Committee)



Ping Chang
(Member)



Neil W. Tindale
(Member)



Gerald R. North
(Head of Department)

August 1996

Major Subject: Meteorology

ABSTRACT

Particle Dispersion within Zonal Jets
in Two-Layer Beta-Plane Turbulence. (August 1996)

Jennifer Claire Roman, B. S., University of Arizona

Chair of Advisory Committee: Dr. R. Lee Panetta

Passive tracer dispersion is studied in a two-layer, quasigeostrophic, beta-plane model in which persistent, steady, zonal jets are observed. Particle trajectories and statistics are examined for barriers to or mechanisms for mixing. Simulations are performed for two different values of the planetary vorticity gradient, and an Eulerian energy timescale and a lengthscale dependent on the number of jets in the flow are developed to enable comparison between the two systems. Using this new timescale and lengthscale, it is shown that zonal particle root-mean-square displacements are enhanced as β increases, and meridional rms displacements in regions away from wave-breaking activity are unaffected by an increase in the planetary vorticity gradient. Two-particle spreading also increases with β . Larger values of beta result in diminished Rossby wave-breaking on the maximum gradient of potential vorticity associated with jet cores, so that tracer dispersion across westerly jets is decreased.

The dependence of tracer statistics on the scales of waves included in the advecting flow is also examined. Hyperviscosity, rather than laminar or biharmonic diffusion, is used to parameterize dissipation in the model, so that enstrophy is allowed

to cascade to small scales. As a result, single- and two-particle statistics do show a dependence on the number of small scale waves included, and in particular, it is shown that removal of small scales increases zonal displacements and inhibits meridional displacements. This is thought to be a result of the decreased Rossby wave-breaking that accompanies the removal of small scales from the advecting flow.

TABLE OF CONTENTS

	Page
ABSTRACT	iii
DEDICATION	v
ACKNOWLEDGEMENTS	vi
TABLE OF CONTENTS	vii
LIST OF TABLES	ix
LIST OF FIGURES	x
CHAPTER	
I INTRODUCTION	1
II BACKGROUND	5
Turbulent Diffusion	5
Potential Vorticity and Passive Tracers	9
Rossby Wave-breaking	11
III MODEL DESCRIPTION	13
Eulerian Flow	13
Lagrangian Fields	16
Statistical Analysis	19
IV SIMULATIONS AND DISCUSSION	22
Effect of the Planetary Vorticity Gradient	22
Scale Sensitivity	41
V SUMMARY AND CONCLUSIONS	69
REFERENCES	71

	Page
APPENDIX	73
VITA	77

LIST OF TABLES

TABLE		Page
1	Parameters for the two beta cases	22
2	Parameters used in scale sensitivity simulations	41
3	Lagrangian integral timescales for the scale sensitivity simulations	62

LIST OF FIGURES

FIGURE		Page
1	Spin-up and equilibration energy levels	17
2	Zonally averaged lower-layer transient eddy zonal flow	17
3	Single-particle displacements for $\beta=.25$	24
4	As in figure 3 but for $\beta=.4$	25
5	Two-particle displacements for $\beta=.25$	27
6	As in figure 5 but for $\beta=.4$	28
7	Tracer trajectories for $\beta=.25$ at $10T_E$	30
8	Tracer trajectories for $\beta=.4$ at $10T_E$	30
9	As in figure 7 but for $20T_E$	31
10	As in figure 8 but for $20T_E$	31
11	As in figure 7 but for $30T_E$	32
12	As in figure 8 but for $30T_E$	32
13	Potential vorticity field for $\beta=.25$ at time step 2	34
14	As in figure 13 but for time step 3	35
15	As in figure 13 but for time step 4	36
16	Potential vorticity field for $\beta=.4$ at time step 2	37
17	As in figure 16 but for time step 3	38
18	As in figure 16 but for time step 4	39

FIGURE		Page
19	Initial potential vorticity field for $K_{co} = 60$	42
20	As in figure 19 but for $K_{co} = 20$	42
21	As in figure 19 but for $K_{co} = 10$	43
22	As in figure 19 but for $K_{co} = 5$	43
23	Single-particle displacements for $K_{co} = 60$	45
24	As in figure 23 but for $K_{co} = 20$	46
25	As in figure 23 but for $K_{co} = 10$	47
26	As in figure 23 but for $K_{co} = 5$	48
27	Two-particle displacements for $K_{co} = 60$	50
28	As in figure 27 but for $K_{co} = 20$	51
29	As in figure 27 but for $K_{co} = 10$	52
30	As in figure 27 but for $K_{co} = 5$	53
31	Maximum meridional excursions for $K_{co} = 60$	55
32	As in figure 31 but for $K_{co} = 20$	56
33	As in figure 31 but for $K_{co} = 10$	57
34	As in figure 31 but for $K_{co} = 5$	58
35	Zonal velocity autocorrelations for the four cases	60
36	As in figure 35 but for meridional velocities	61
37	Wave-breaking time series for $K_{co} = 60$	63

FIGURE		Page
38	As in figure 37 but for $K_{co}=20$	64
39	As in figure 37 but for $K_{co}=10$	65
40	As in figure 37 but for $K_{co}=5$	66

CHAPTER I

INTRODUCTION

Although it is difficult to give an exact definition of turbulence, we may gain insight into turbulent flow by examining some of its characteristics: irregular behavior, intermittancy, nonlinearity and strong mixing. Of these, the most important feature of turbulence is its diffusivity, or mixing ability (Tennekes and Lumley 1972). Simple dimensional analysis shows that the rate of diffusion due to turbulent motions is several orders of magnitude larger than the molecular diffusion rate. Given an *isotropic* ($\beta = 0$) flow with eddy velocity \vec{V}' , the “eddy diffusivity” κ_T is defined by

$$\overline{\vec{V}'\theta'} = \kappa_T \nabla \bar{\theta}$$

where θ is some quantity of interest (i.e., heat). This expression may be written as

$$\kappa_T \approx (|\vec{V}' \cdot \theta'|)/(|\nabla \theta|)$$

and dimensional analysis yields

$$\kappa_T \approx (U\theta)/(\theta/L) = UL.$$

The ratio of the eddy diffusivity to the molecular diffusivity, ν , can now be written

This thesis follows the style and format of *Journal of the Atmospheric Sciences*.

$$\kappa_T/\nu \approx UL/\nu = Re$$

where Re is the Reynolds number of the flow. Thus, the Reynolds number of a turbulent flow can be thought of as the ratio of molecular diffusion to turbulent diffusion, and in order for the Reynolds number to be large, a necessary condition for turbulent flows, ν must be much less than κ_T . In *anisotropic* turbulent flows, such as the ones studied in this research, κ_T is direction-dependent, and its value is proportional to the flux in a particular direction divided by the gradient in that direction. Thus, the eddy diffusivity in the zonal direction could be very different than the eddy diffusivity in the meridional direction. In both isotropic and anisotropic flows, however, turbulence is an expedient means of mixing and a robust mechanism for transport of tracers such as potential vorticity, passive contaminants and heat.

The presence of zonal jets in a flow has varying effects on transport depending upon whether the tracer is active or passive (an active tracer interacts with the surrounding flow, whereas a passive, or dynamically inactive, tracer is merely carried along by it). Eddy-forced zonal jets tend to coincide with regions of increased meridional transport of heat, an *active* tracer. In the troposphere, the stormtracks associated with jets are a major region of poleward transient eddy heat transport (Holton 1992); the thermal wind balance requires a strong meridional temperature gradient to be consistent with the strong vertical shear in jets. The dispersion of *passive* tracers, however, has been numerically (Pierrehumbert 1991a; Bowman and

Chen 1993), experimentally (Sommeria *et. al.* 1989), and observationally (Bowman 1993) shown to be suppressed in the meridional direction in the presence of zonal jets. The laminar jets are sites of very little mixing and become barriers to passive tracer transport, resulting in anisotropic dispersion with zonal trajectories favored over meridional trajectories. In the case of the Antarctic polar vortex, the barrier to mixing plays a crucial role in separating the ozone-depleted air over the pole from the ozone-rich air at lower latitudes.

The polar vortex and other jets have been found to be *permeable* barriers, however, due to wave-breaking events. In the stratosphere, Rossby waves break on the edge of the polar vortex, ejecting polar air into the midlatitudes where it is mixed away (McIntyre and Palmer 1983). Wave-breaking has also been observed along jets in the upper troposphere, and along the Gulf Stream (Nakamura and Plumb 1994). In each case, the transfer of material across the jet core is irreversible (that is what defines *wave-breaking*), and the penetrability of the jet is related to the frequency and type of wave-breaking events.

This research seeks to further the understanding of passive tracer dispersion in a system that combines the efficiency of transport in turbulent flows, the general anisotropy of transport in the presence of jets, and the episodic nature of transport associated with Rossby wave-breaking. Efforts are concentrated in two main areas: a description of zonal and meridional transport, and the dependence of transport on

wave scale.

The first objective seeks to qualitatively and quantitatively describe the dependence of tracer dispersion on the value of the planetary vorticity gradient. Due to the nondimensionalization of the model, the model parameter β is proportional to the inverse of the vertical shear, i.e., increasing beta is equivalent to decreasing the vertical shear, or decreasing the meridional temperature gradient. In this research, two values of beta are examined that equate to a strong and moderate horizontal temperature gradient/vertical shear. Particle trajectories and statistics are examined for barriers to or mechanisms for mixing, and efforts focus primarily on understanding meridional dispersion.

The second objective describes the dependence of tracer transport on the scales of waves included in the background flow. In some simulations, only certain wavenumbers are retained and experiments are repeated. Removal of small scale waves is equivalent to a coarsening of grid-point separation. Results should determine which scales dominate particle dispersion for this system, and show that accurate characterization of tracer transport depends upon the resolution of the observational network.

CHAPTER II

BACKGROUND

Turbulent Diffusion

Taylor (1921) was the first to extract Lagrangian statistics from an Eulerian turbulent flow. Examining homogeneous, isotropic turbulence, he derived a relationship between single-particle displacements and the time of particle migration, T , based upon velocity autocorrelation arguments. Taylor found that for short time intervals, when T is so small that the velocity of the flow changes little as the particle is advected, the standard deviation of a tracer from its initial position is proportional to T . For long migration times, when changes in flow velocity are substantial, tracer dispersion increases as \sqrt{T} . Such long-term behavior is termed "random walk". Taylor's (and his colleagues') work in the field of turbulent diffusion was necessarily limited to "simple" flows since Lagrangian statistics could only be obtained experimentally, requiring that measurements be taken following a randomly moving fluid particle. Not until computers allowed the possibility of numerically simulated turbulent flows were higher-order Lagrangian statistics easily obtained.

Riley and Patterson (1974) were the first to examine decaying, isotropic turbulence by numerically integrating the Navier-Stokes equation, in an attempt to relate Eulerian velocity information to Lagrangian velocity statistics. They were able to reproduce Taylor's autocorrelation-based results for single-particle displacements, but

more importantly, were able to calculate and compare the velocity autocorrelations for the tracers and the flow field. Their results showed that the Lagrangian autocorrelation coefficient, R_L , at short time lags ($\tau < 100\Delta t$), is larger than the Eulerian autocorrelation coefficient, R_E , which means the tracers are more persistent in holding their initial conditions than is the flow field. At long time lags ($\tau > 100\delta t$), however, R_L is less than R_E , implying that the tracers undergo a greater “memory loss” during this stage of transport than does the mean flow. Huang and Leonard (1995) repeated these results, and attributed the long-time behavior to differences in the energy levels of low-frequency eddies present in the Eulerian and Lagrangian frames of reference. ($R_E > R_L$ implies more energy is present in Eulerian low-frequency eddies than in Lagrangian ones.) Huang and Leonard also examined other higher-order Lagrangian statistics and found a self-preserving Lagrangian velocity autocorrelation coefficient that allows prediction of particle dispersion rates (based upon an eddy length scale, turbulent velocity, and dissipation rate) in systems with a power-law decay of turbulent energy. Yeung and Pope (1989) performed several experiments on stationary, homogeneous, isotropic turbulence and concluded that Lagrangian one-particle statistics are particularly affected by the motions of the large-scale flow, which may be sensitive to model forcing and boundary conditions. (In the model used in this research, however, effects of boundary conditions have been minimized). Yeung and Pope also showed that low-order Lagrangian statistics, such as velocity autocorrela-

tion coefficients and rms displacements, are not particularly sensitive to the Reynolds number of the flow.

While the previous studies examined isotropic turbulence, Haidvogel (1982, 1985) studied particle dispersion in numerically integrated homogeneous, β -plane turbulence. Haidvogel determined that Lagrangian statistics are affected by the value of the planetary vorticity gradient. As β increases, flows transition from turbulent to wavelike regimes, and zonally-oriented paths develop in the streamfunction and vorticity fields. Zonal single-particle dispersion is enhanced with increased beta, and dispersions in the meridional direction are suppressed. This “anomalous” diffusion, or deviation from random walk behavior, is also expected in models with zonal jets, with superdiffusive behavior zonally, and subdiffusive behavior meridionally. In the atmosphere, the superdiffusivities of tracers in regions with zonal jets may account for the long-range transport of crustal aerosols from their continental source regions, in cases when distances over which the aerosols are transported are much larger than those expected from synoptic winds and settling mechanisms (Ellis and Merrill 1995). Subdiffusive meridional transport of tracers in regions of zonal jets is expected based on conservation of potential vorticity arguments (see below). In a personal communication, Hua stated that her results (in a system similar to the one used in this research) indicated globally averaged *meridional* transport could best be described by random walk, i.e., there were no anomalies in transport due to the presence of

jets. These results may be due to statistical averaging of the broad, weak easterly jet regions with the narrow, strong westerly jet regions. This research will attempt to further quantify inhomogeneities in the meridional diffusivity.

Haidvogel's statistical results show clearly the effect of beta on tracer transport. Lagrangian velocity autocorrelation coefficients become strongly anisotropic as the planetary vorticity gradient is increased, and at very high β , the zonal correlation does not reach zero throughout the period of integration. The beta-effect is similarly seen in rms displacement curves. While short-time behavior of particle dispersion on a β -plane continues to be proportional to time T (as in the isotropic case), long-time behavior exhibits anisotropy. Zonal dispersion remains correlated so that single-particle displacements grow at a rate larger than \sqrt{T} , but meridional dispersion grows at a slower rate. As β increases, the zonal displacement rate approaches T , while the meridional rate becomes very nearly zero.

Finally, Haidvogel showed that inclusion of only the large-scale waves ($K \geq 10$) in the Eulerian velocity fields has no effect on the one-particle statistics, implying that the rms displacement is controlled by the larger eddies, as suggested by Yeung and Pope. Haidvogel's simulations were performed using laminar (∇^2 on vorticity) diffusion, however, so that most of the enstrophy was dissipated before reaching small scales. The model used in this research parameterizes the small-scale diffusion using hyperviscosity (∇^8 on vorticity) in order to push the viscosity to much smaller

scales (allowing a true enstrophy cascade). Part of this research will be devoted to understanding which scales of motion must be included in this model in order to correctly characterize the tracer dispersion.

Potential Vorticity and Passive Tracers

Haidvogel also examined the conservation of potential vorticity following particle trajectories. Potential vorticity (p.v.) conservation refers to the ability to account for all changes in p.v. along a tracer trajectory, and to associate the changes with effects of dissipation and forcing. Haidvogel found that tracers experienced unexplainable changes in their p.v. values shortly after initialization, and vorticity was in no way approximately conserved. His simulation used a highly accurate interpolation scheme for particle advection to minimize interpolation error, so discrepancies in p.v. conservation were attributed to truncation of the Eulerian flow (used in the dealiasing algorithm). This truncation (determined by model resolution) forces nonlinear interactions with wavenumbers higher than K_{max} to be ignored, resulting in removal of an important component of the Lagrangian vorticity balance. This suggests that spatial resolution is important to the actual paths the tracers follow, as shown by Hua (1994), with higher resolution resulting in “truer” paths. However, the truncation has minimal impact when one-particle Lagrangian statistics are computed, since these statistics are controlled by the large-scale energy-containing eddies

($K \ll K_{max}$). Thus, in any study of tracer dispersion, the trajectories of the particles may be in question, but the single-particle statistics derived from the tracer positions and velocities should not be.

Pierrehumbert (1991a, 1991b) further qualified the relationship between potential vorticity, its gradients, and tracer transport, by examining the effects of large-scale two-dimensional flows on the mixing of tracers and p.v. He found that the characteristic mixing zones and barriers to transport that evolved in the tracer fields were also evident in the potential vorticity fields. Although coherent regions of p.v. may resist spreading due to their inherent roll-up and rotation, as long as they are not so concentrated that the flow cannot tear them apart, they may be treated as passive tracers. Thus, in contrast to the traditional view that potential vorticity gradients are barriers to mixing, Pierrehumbert asserts (1991a) that a strong p.v. gradient is a *signature* of a mixing barrier in the flow. We may then presume that where strong zonal gradients in p.v. are present, meridional dispersion may be suppressed.

In the model of zonal jets to be used in this research (Panetta 1993), potential vorticity gradients are strongest in the core of westerly jets. This implies that tracers should encounter a barrier to meridional transport in westerlies. As will be shown, however, the barrier is rendered permeable by wave-breaking.

Rossby Wave-breaking

The relationship of Rossby wave-breaking to tracer transport gained importance in light of its implications for ozone chemistry. McIntyre and Palmer (1983) showed that wave-breaking along the stratospheric polar vortex results in ejection of material within the vortex into the midlatitudes. Using potential vorticity as their tracer, Juckes and McIntyre (1987) simulated the process of wave-breaking by numerically integrating a high-resolution, one-layer hemispheric model representing the winter stratosphere. Their results showed that some of the thin filaments of potential vorticity, created by wave-breaking, roll up into vortices, while some filaments remain elongated and act as if the p.v. were a passive tracer. In either case, high p.v. air from inside the polar vortex was ejected into lower latitudes, and the vortex was eroded.

Polvani and Plumb (1992) further classified wave-breaking using the Contour Dynamics method on a single-contour vortex. They asserted that there exists a forcing threshold above which breaking results in “dynamically significant” changes to the vortex. Below this threshold, however, breaking results in weak filaments of material being stripped from the vortex. As the vortex is not changed substantially, Polvani and Plumb label this sub-threshold behavior *microbreaking*. It may be surmised then, that passive tracer transport across a jet may be larger in cases of Rossby wave *breaking*, rather than *microbreaking*.

The models used by Juckes and McIntyre, and Polvani and Plumb both exhibited wave-breaking only on the equatorward side of the stratospheric vortex, and the asymmetry was attributed to a similar one-sidedness in the strain rate distribution (largest on the equatorward side of the jet due to jet curvature). For this reason, Nakamura and Plumb (1994) examined wave-breaking on a straight jet, and found that the direction of breaking depends on the shear of the flow on either side of the jet. In particular, when the shear field is symmetric about the jet, wave-breaking occurs on both sides; otherwise, wave-breaking is stronger on the side of the jet with the largest shear. The direction of wave-breaking will, of course, have an impact on the direction of tracer dispersion, and subsequent reversibility of the transport.

Recently, Bowman (1995) proposed a relationship between dispersion of particles by wave-breaking and molecular diffusion of the tracers. His work with an isentropic stratospheric model showed that when a region of flow that contained tracers was repeatedly subjected to wave-breaking, the resultant transport resembled random walk, or molecular diffusion. He related the timescale of transport to the frequency of the wave-breaking events, and showed that meridional dispersion of tracers in wave-breaking regions was linear in time.

It is clear, then, that any study of tracer transport in a system that contains Rossby wave-breaking, must account for the frequency of wave-breaking events. It is unclear, however, how to measure this quantity in the model used in this research.

CHAPTER III

MODEL DESCRIPTION

This research investigates the dispersion of passive tracers in and around zonal jets. These jets are simulated using a two-layer, quasigeostrophic model run under certain parameters. After the Eulerian flow including the jets reaches a statistically steady state, tracers are initialized into the flow, and are advected for 50 nondimensional “model days.” Tracer positions and velocities are stored at each time step for use in statistical calculations.

Eulerian Flow

The Eulerian flow is generated by a two-layer, quasigeostrophic, beta-plane model, such as that discussed in Panetta (1993) and Pedlosky (1987). The domain is doubly-periodic in order to eliminate any boundary effects on the flow, and bottom topography is not included. The two layers have equal resting depths, H , and the lower layer is slightly more dense than the upper layer. The spatial resolution of the model may be 128^2 or 256^2 grid points, superposed on a domain that is $2\pi L$ Rossby radii on a side, where L equals 15 or 10, depending on the simulation. The large computational domain is necessary to resolve the narrow spectral peaks in the flow resulting from the jets (the spectral resolution for a $2\pi L$ domain is $1/L$.)

The model is started with a small amount of energy, introduced by initial-

izing a band of linearly unstable waves whose amplitudes and phases are centered spectrally around the wavenumber of maximum instability. The energy source for “eddy” motions, or deviations from the mean flow, is the potential energy reservoir inherent in the time-invariant, domain-averaged vertical shear in the zonal wind. In order to generate the zonal jets and their accompanying “storm tracks,” the model is run under a specific set of parameters, including (a) a forcing mechanism provided by the assumed horizontally uniform, unstable vertical shear, (b) a background gradient of potential vorticity, and (c) weak damping that allows nonlinear effects to dominate. Damping may be provided through surface drag or hyperviscosity. (In this respect, the model differs from that of Panetta [1993], which included *biharmonic* diffusion.)

The potential vorticity for layer i , where $i = 1$ is the upper layer and $i = 2$ is the lower layer, may be written in terms of the dimensional streamfunction Ψ_i^* as

$$Q_i^* = (f_0^* + \beta^* y^*) + (\nabla^2 \Psi_i^* + (-1)^i \hat{\Psi}^* / \lambda^2)$$

where $\hat{\Psi}^* = (\Psi_1^* - \Psi_2^*)/2$, and the internal Rossby radius is defined by $\lambda = [g(\rho_2 - \rho_1)H/(2\rho_2 f_0)]^{1/2}$. The evolution equations for potential vorticity in the two-layer, quasigeostrophic, beta-plane model can be written

$$\partial Q_1^* / \partial t^* + J(\Psi_1^*, Q_1^*) = -\nu^* \nabla^{10} \Psi_1^* \quad (1a)$$

$$\partial Q_2^* / \partial t^* + J(\Psi_2^*, Q_2^*) = -\kappa_M^* \nabla^2 \Psi_2^* - \nu^* \nabla^{10} \Psi_2^*. \quad (1b)$$

The horizontal Jacobian is denoted by $J(., .)$, ∇^2 is the horizontal Laplacian operator,

κ_M^* is mechanical damping (surface drag or Ekman pumping), and ν^* is small-scale mixing.

Because the transport of tracers by the eddy field is of interest in this research, the streamfunctions for the two layers are decomposed into mean and eddy flow components

$$\Psi_1^*(x^*, y^*, t^*) = \psi_1^*(x^*, y^*, t^*) - U_0 y^* \quad (1c)$$

$$\Psi_2^*(x^*, y^*, t^*) = \psi_2^*(x^*, y^*, t^*). \quad (1d)$$

The streamfunctions ψ_i^* are deviations from the time-invariant state with a horizontally uniform vertical shear in the zonal flow, U_0 . It is assumed the lower layer is at rest (or the reference frame is travelling at the speed of the lower layer).

Substitution of (1c) and (1d), followed by nondimensionalization (see appendix), result in expressions for the evolution of the nondimensional eddy potential vorticity fields

$$\partial q_1 / \partial t + J(\psi_1, q_1) = -\partial q_1 / \partial x - (\beta + \frac{1}{2}) \partial \psi_1 / \partial x - \nu \nabla^{10} \psi_1 \quad (2a)$$

$$\partial q_2 / \partial t + J(\psi_2, q_2) = -(\beta + \frac{1}{2}) \partial \psi_2 / \partial x - \kappa_M \nabla^2 \psi_2 - \nu \nabla^{10} \psi_2. \quad (2b)$$

These equations form the basis for the pseudo-spectral numerical model. They are integrated using a leapfrog scheme, with periodic application of a leapfrog-trapezoidal timestep to eliminate the computational mode. Nonlinear velocity products are evaluated in physical space and then transformed to spectral space for integrations. A

circular truncation is used and calculations are dealiased using the method of Orszag (1971).

During each simulation, the model is allowed to run several hundreds to thousands of model days until spin-up and equilibration are complete (see Panetta 1993) and the zonally averaged energy levels show the flow to be statistically steady. Figures 1 and 2 show examples of the zonally averaged zonal velocity field and the associated energy levels, as the system passes through spin-up and equilibration, reaching a statistically steady state by the end of the period. During spin-up the energy levels grow rapidly, eventually reaching a state where levels oscillate about some mean value. Correspondingly, the zonally averaged flow undergoes a period of jet building and merging, until finally, five steady jets appear.

Lagrangian Fields

Once the background flow has reached the steady state, point tracers are initialized into each layer of the flow field. The particles are released with various initial configurations, depending on which part of the flow is being examined; i.e., the tracers may be deployed inside the westerly jets, inside the easterlies, or on equally-spaced grid points throughout the domain.

In each case, the particle trajectories are obtained using the Eulerian eddy velocities at the positions of the tracers (i.e., Lagrangian frame of reference moves

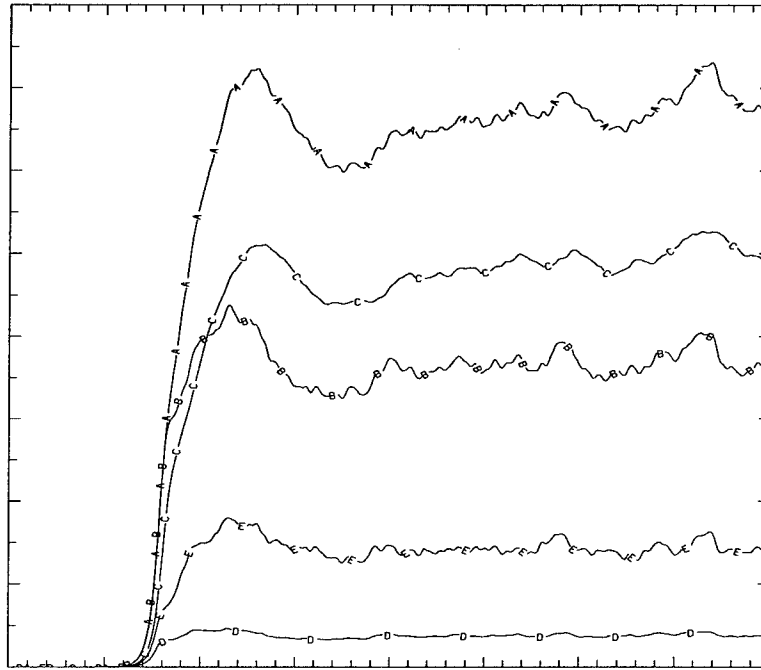


Figure 1 Spin-up and equilibration energy levels. Energy magnitude on ordinate, time on abscissa.

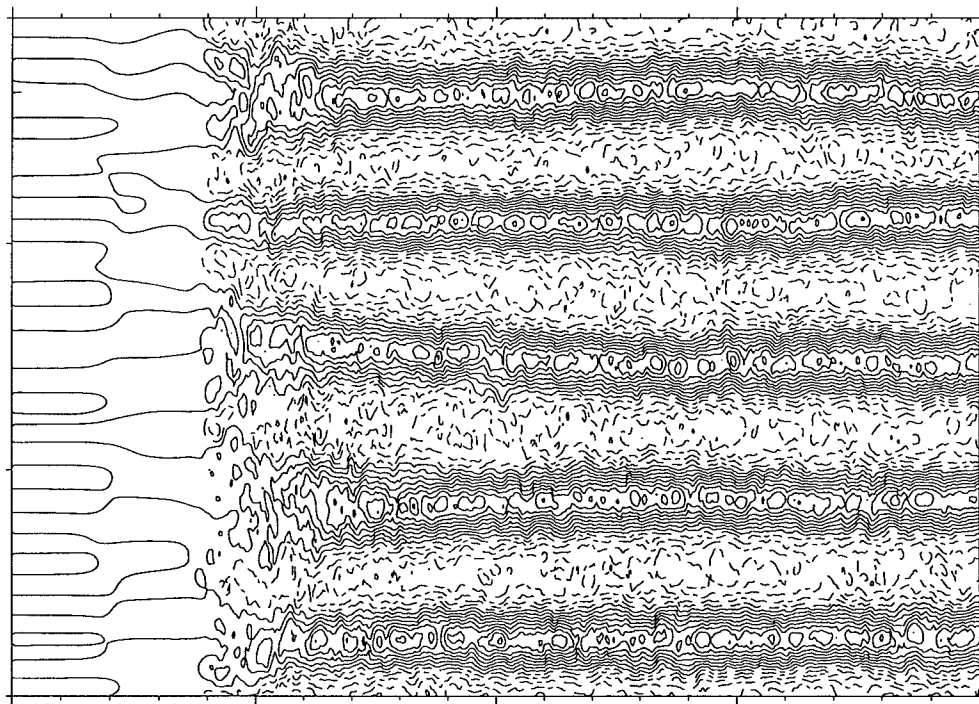


Figure 2 Zonally averaged lower-layer transient eddy zonal flow. Meridional distance on ordinate, time on abscissa.

with the mean background flow):

$$d\vec{x}_p/dt = \vec{v}(\vec{x}_p, t), \quad p = 1, mtra$$

where *mtra* is the maximum number of tracers initialized in the flow. The Eulerian eddy velocity fields are interpolated from the grid points to the position of the tracer by fitting a streamfunction to the velocity field over the neighboring 16 (4x4) grid points and using a third-order Lagrange interpolation to find the value of the streamfunction (velocity) at the tracer position, as in Hua (1994). The evolution of observed potential vorticity of each tracer is also calculated using the 16 point Lagrange interpolation.

Once the tracer velocities are calculated for a particular timestep, the particle positions are integrated forward in time using a fourth-order Runge-Kutta scheme. For successive timesteps, n and $n + 1$, the position of the tracer at $n + 1$ is given by

$$x_{n+1}^{\vec{}} = x_n^{\vec{}} + \frac{1}{6}(\vec{k}_1 + 2\vec{k}_2 + 2\vec{k}_3 + \vec{k}_4)$$

for

$$\vec{k}_1 = \delta t \vec{v}(\vec{x}_n, t_n)$$

$$\vec{k}_2 = \delta t \vec{v}(\vec{x}_n + \frac{1}{2}\vec{k}_1, t_n + \frac{1}{2}\delta t)$$

$$\vec{k}_3 = \delta t \vec{v}(\vec{x}_n + \frac{1}{2}\vec{k}_2, t_n + \frac{1}{2}\delta t)$$

$$\vec{k}_4 = \delta t \vec{v}(\vec{x}_n + \vec{k}_3, t_n + \delta t)$$

where δt is the time step interval. The tracers are advected for 50 model days for each simulation, allowing the eddies to evolve through several turnover times.

Statistical Analysis

Time series of tracer positions and vorticities are stored during advection, and this data is used to perform the Lagrangian statistical analysis. Statistics calculated by the model include the velocity autocorrelation coefficients, root-mean-square single-particle displacements and two-particle relative displacements.

As a particle moves away from some initial position, it will become decorrelated from the conditions existing at the starting point, or will “lose” its memory of the initial conditions. A measure of this memory loss is the Lagrangian velocity autocorrelation coefficient, which may be written

$$R_L(\tau) = \left\langle \frac{\int \alpha(p,t) \alpha(p,t+\tau) dt}{\sigma_p(t) \sigma_p(t+\tau)} \right\rangle$$

$$\sigma_p(T) = \sqrt{\langle [\alpha(p,T)]^2 \rangle}, \quad T = t \text{ or } t + \tau$$

where each integral is evaluated over all time lags $0 \leq \tau \leq \text{maxlag}$. Brackets $\langle \rangle$ represent an ensemble average over all tracers particles, $1 \leq p \leq \text{mtra}$. The quantity $\alpha_p(\tau)$ used in the autocorrelation calculation is the deviation from the mean, calculated by removing the average (over all particles) of α_p at that time lag. In this research, autocorrelations were calculated separately for $\alpha_p = u_p$ (the zonal velocity of the particles) and $\alpha_p = v_p$ (the meridional velocity) in each layer. Thus, a com-

parison may be made between the along-jet and cross-jet decorrelation times. These decorrelation times, or Lagrangian integral time scales, are defined as the integrals of the autocorrelation curves over the total time of integration. In this research, we expect zonal velocity autocorrelation times to be longer than meridional velocity autocorrelation times, since, in the presence of zonal jets, it is easier for a particle to retain its initial east/west motion than its north/south motion.

Another useful statistic is the rate at which a particle wanders from its initial position. This single-particle spreading rate, or rms displacement, may be written

$$D_x(t) = \langle x_p'(t)^2 \rangle^{1/2} = \langle [x_p(t) - x_p(0)]^2 \rangle^{1/2}$$

$$D_y(t) = \langle y_p'(t)^2 \rangle^{1/2} = \langle [y_p(t) - y_p(0)]^2 \rangle^{1/2}$$

where again, the angle brackets mean an ensemble average over all particles. The rms displacement at the Lagrangian integral time scale may be used as an estimate of the Lagrangian integral length scale, or the distance a particle travels before it completely loses its “memory” of initial conditions. In a flow dominated by easterly and westerly jets, it is expected that zonal displacements over a certain length of time should exceed meridional displacements.

A third statistic of interest is the two-particle spreading, or average relative separation, defined as

$$R^2(t) = \langle |\vec{x}_p(t) - \vec{x}_s(t)|^2 \rangle$$

where the ensemble average is taken over all particle pairs (p, s) with a certain initial separation. This statistic examines only the magnitude of separation, not orientation, and is controlled by the flow shear rather than the flow velocity (Haidvogel 1985).

While these and other statistics were examined, none satisfactorily represented the nature of the meridional dispersion of tracers. This dispersion will be shown to depend upon the frequency of wave-breaking in the complex background flow, a quantity which we as yet have no means to measure. The aforementioned statistics do, however, lend insight into other aspects of Lagrangian flow.

CHAPTER IV

SIMULATIONS AND DISCUSSION

Effect of the Planetary Vorticity Gradient

The primary objective of this research was to characterize tracer transport among zonal jets on a beta-plane. This was accomplished by examining particle trajectories and statistics for the two simulations listed in Table 1. These parameters were chosen to show the effect of the planetary vorticity gradient on tracer dispersion.

Since the value of beta effects the energy level of the flow (energy increases as beta decreases), a parameter was needed that allowed for relative comparisons of timescales in the two simulations. Thus, an Eulerian timescale was developed by examining the eddy kinetic energies of the two cases. The eddy kinetic energy of a flow is defined as

$$E_e = \int E(K) dK, \quad 0 \leq K \leq K_{max}$$

where K is the total wavenumber. The weighted eddy kinetic energy of a flow is

$$E_w = \int K \cdot E(K) dK.$$

Table 1 Parameters for the two beta cases.

<i>Resol.</i>	\tilde{L}	β	κ_M	ν	T_E
128^2	10	.40	.05	$8.E10^{-7}$	1.1
256^2	10	.25	.05	$1.E10^{-8}$.74

An Eulerian length scale, l_E , may then be constructed by taking the inverse of (E_w/E_e) . A corresponding Eulerian timescale of the flow, the large eddy turnover time, T_E , may be defined in terms of this length scale by letting

$$T_E = \sqrt{(l_E)^2/E_e} = l_E/\sqrt{E_e} = E_e/(\sqrt{E_e}E_w) = \sqrt{E_e}/E_w.$$

It is this timescale (for the upper layer) that will be used to compare the two cases. The values of T_E (in nondimensional days) for the runs are also listed in Table 1, and it is immediately evident that the flow in the $\beta=.4$ case evolves more slowly than the low-beta case due to the decrease in energy of the flow.

Another difference between the two flows, which must be taken into account for any accurate comparison to be made, is the average distance between the center of the easterlies (where tracers were initialized) and the core of the westerly jets, L_c . This distance gives a characteristic size of eddies imbedded within the easterly flow. In the $\beta=.25$ case, L_c is 15λ (since there are two jets); for $\beta=.4$, it is 7.9λ (for four jets). The differing average jet core separations are used to relate dispersion lengths in the two simulations.

Figures 3 and 4 show the upper-layer, ensemble-average single-particle displacements as a function of *nondimensional* time (model days), for the $\beta=.25$ and $\beta=.4$ cases, respectively. The average zonal dispersion is indicated by curve A, and curve B shows meridional dispersion. Again, to correctly compare the two figures, the values for rms displacements at certain multiples of T_E were examined. Figure

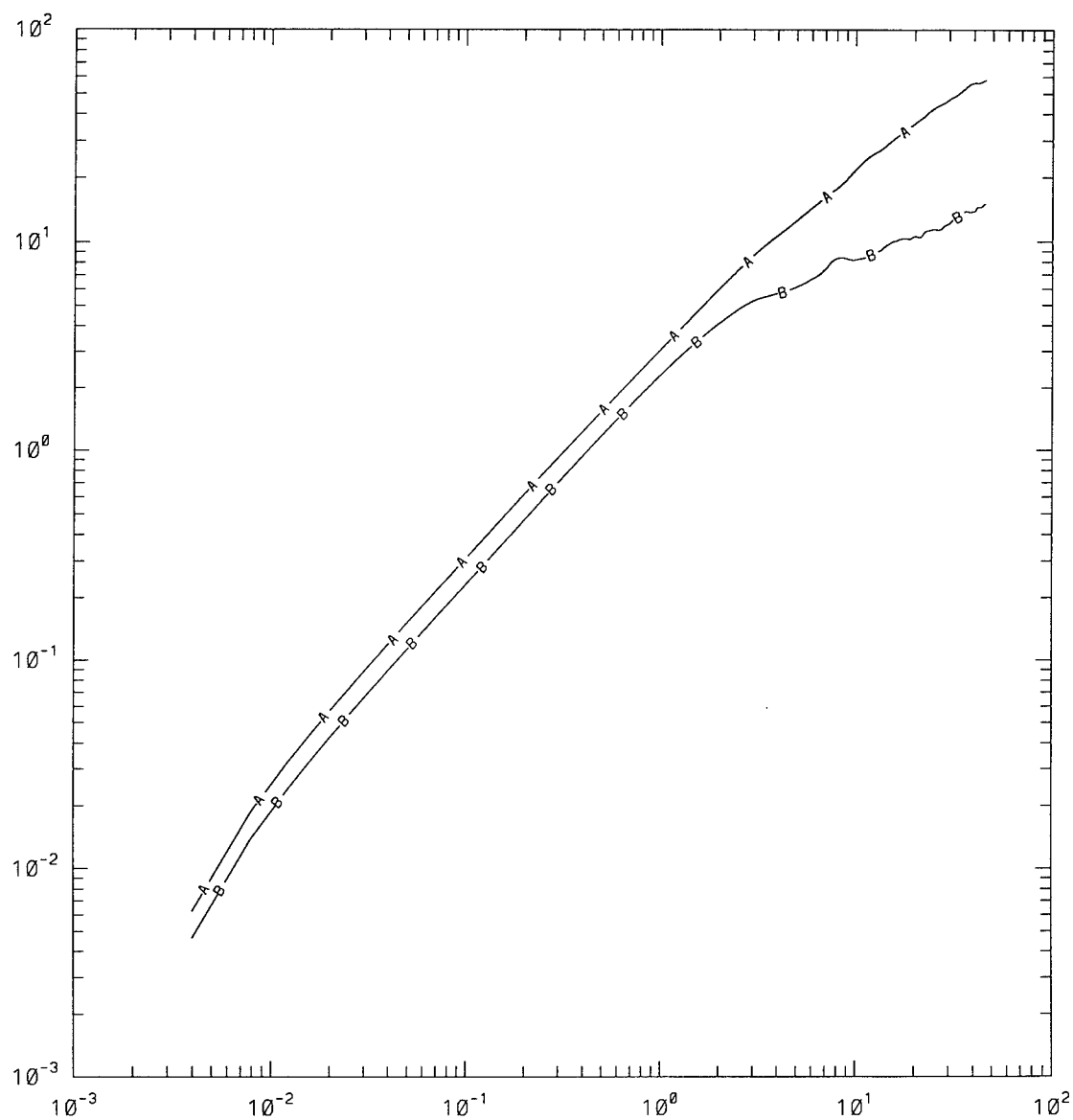


Figure 3 Single-particle displacements for $\beta=.25$. Log of displacement in λ on ordinate, log of nondimensional time on abscissa. Curve A is zonal displacements, curve B is meridional displacements.

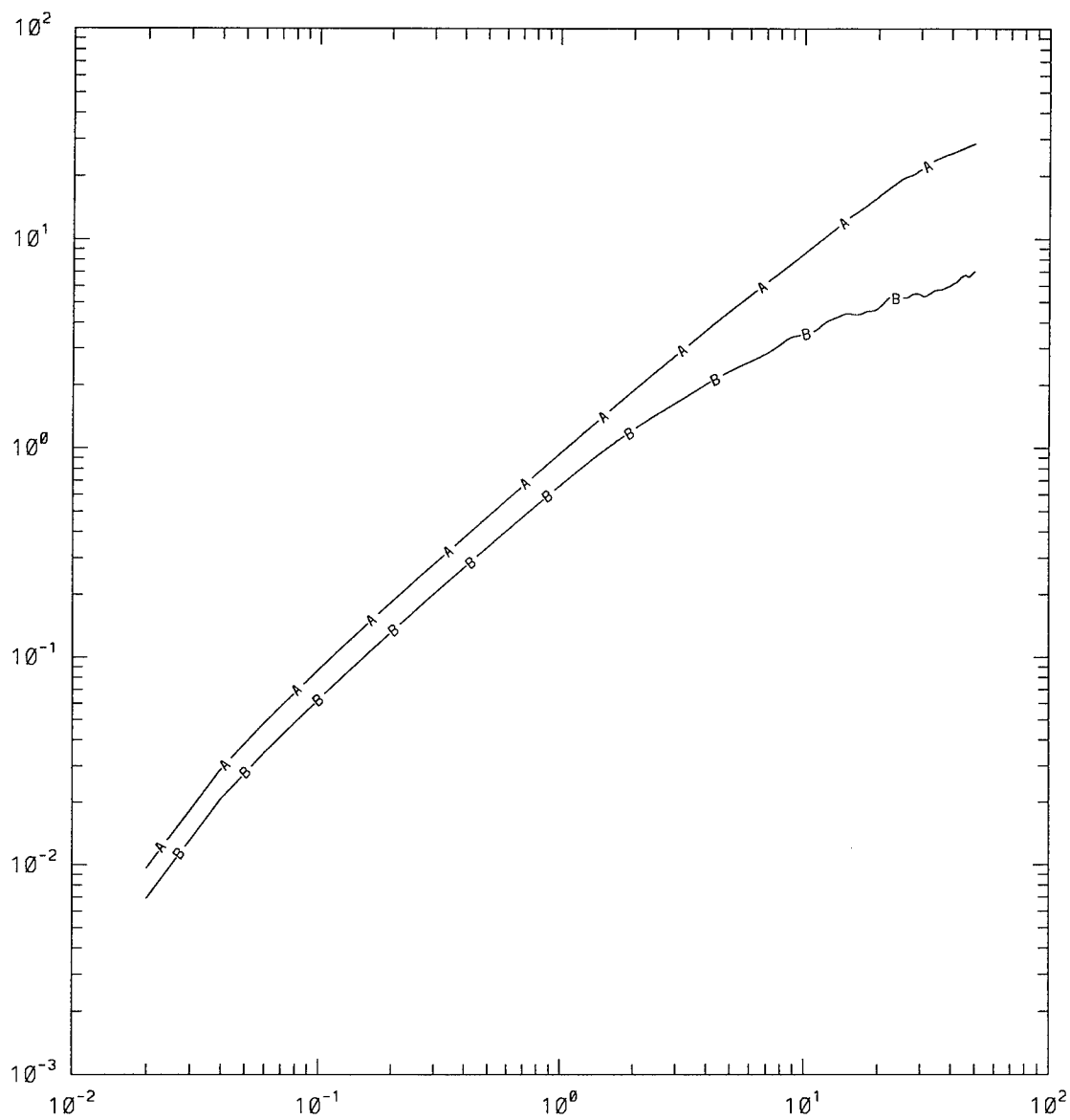


Figure 4 As in figure 3 but for $\beta=.4$.

3 shows that the zonal rms displacement for the $\beta=.25$ case is approximately 15λ , or one-quarter of the domain, after ten turnover times. After twenty T_E , the zonal rms displacement for the same case is 30λ , or almost half a domain. From figure 4, it is seen that the zonal rms displacement for the $\beta=.4$ case is 10.5λ after ten turnover times, and 18λ after $20T_e$. These values seem to indicate that increasing the planetary vorticity gradient *decreases* the average single-particle dispersion in a flow. However, when the zonal displacements are rescaled by L_c , the rms displacements *increase* slightly with increased beta. After ten T_E , the values of zonal displacement equate to $1.0L_c$ for $\beta=.25$, and $1.3L_c$ for $\beta=.4$. Similarly, after twenty turnover times, particles have been displaced zonally $2.0L_c$ and $2.3L_c$ in the low- and high-beta cases, respectively.

Examining the same two figures, and concentrating on meridional rms displacements, yields different results. In the $\beta=.25$ case, after ten turnover times the average meridional displacement is 7.8λ . In the $\beta=.4$ case, the meridional displacement after $10T_E$ is 4.1λ . Although it seems that particles are displaced farther in the low-beta case, the value of the displacement in both beta cases corresponds to $0.5L_c$. Similarly, after twenty turnover times, tracers in the $\beta=.25$ case were displaced 10λ meridionally, and tracers in the $\beta=.4$ case were displaced 5.2λ . These values correspond to approximately $0.65L_c$ in each system. Thus, unless meridional dispersions are rescaled to account for the number of jets in the domain and the relative energies

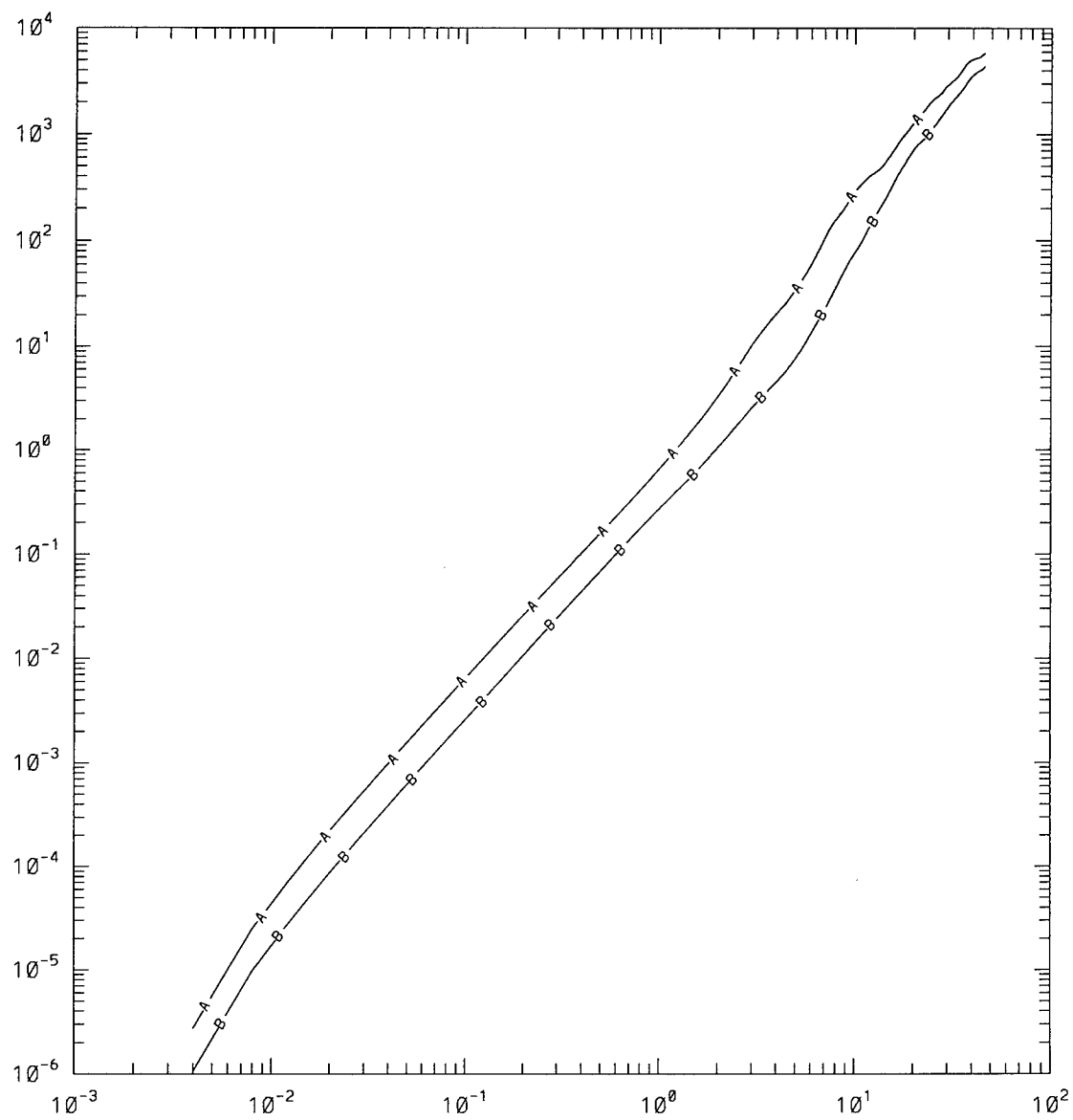


Figure 5 Two-particle displacements for $\beta=.25$. Log of displacement squared in λ on ordinate, log of nondimensional time on abscissa. Curve A is upper-layer displacements, curve B is lower-layer displacements.

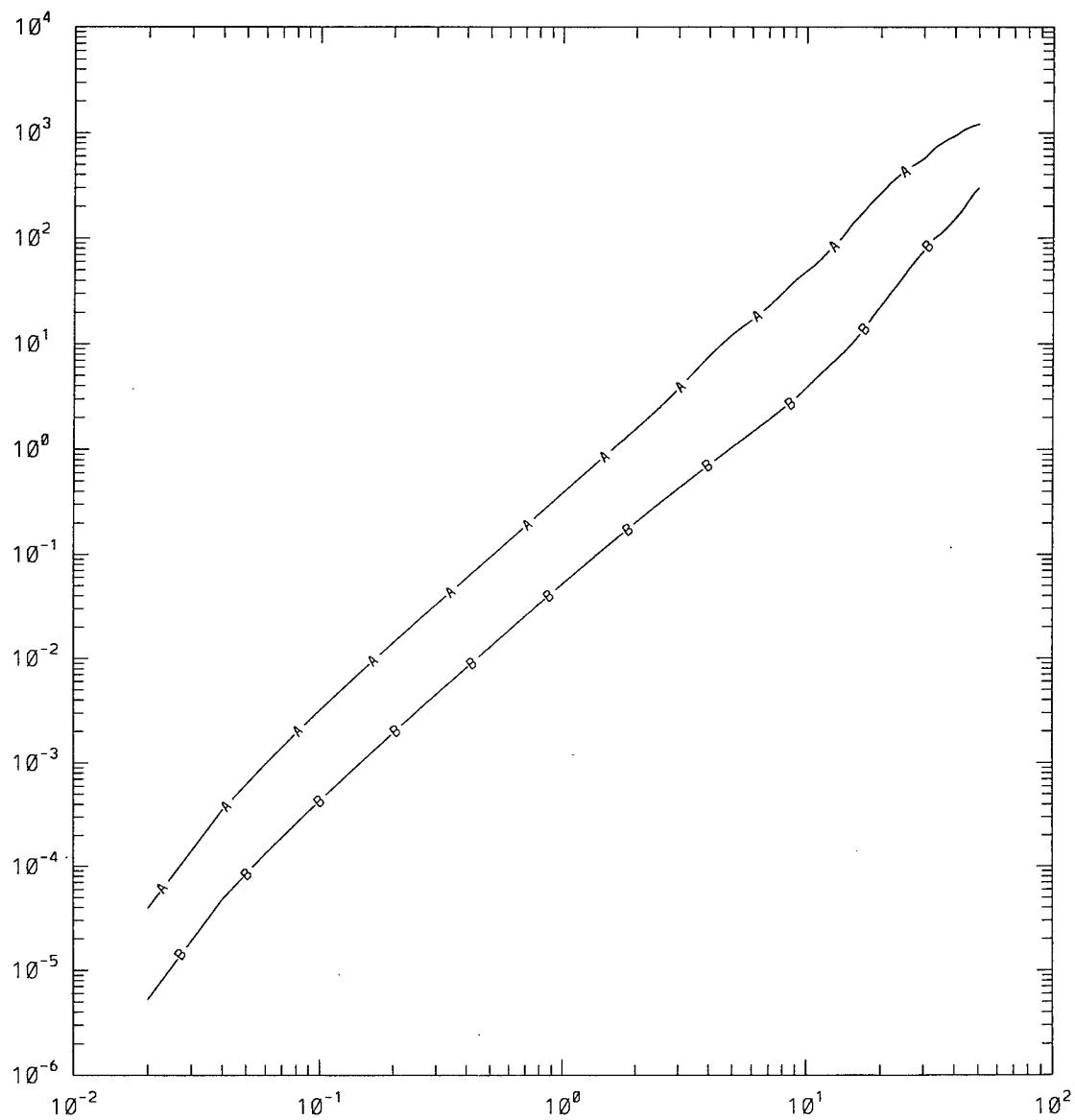


Figure 6 As in figure 5 but for $\beta=4$.

of the flows, it seems that increasing beta acts to decrease meridional dispersions. The rescaling by T_E and L_c , however, indicates that meridional dispersion (in the absence of wave-breaking) is not affected by the value of the planetary vorticity gradient, and zonal dispersion slightly increases with an increase in beta.

Figures 5 and 6 show the two-particle displacement curves for the two beta cases as a function of model days. Curve A represents upper-layer spreading, and curve B represents the lower layer. After $10T_E$ in the upper layer of the $\beta=.25$ case, two particles have spread, on average, 10.5λ , or $0.7L_c$. After the same multiple of turnover times in the $\beta=.4$ case, particles have spread 8.4λ , or $1.1L_c$. The values after twenty turnover times are 26.5λ ($1.8L_c$) for the $\beta=.25$ case, and 20λ ($2.5L_c$) for $\beta=.4$. The results indicate that an increase in beta results in increased particle spreading. Although two-particle statistics show magnitudes of displacement instead of orientations, it is safe to assume that the increase in particle spreading in the $\beta=.4$ case is due to the increase in average zonal displacement in that case.

The next series of figures (figures 7-12) show actual particle trajectories superposed on the zonally-averaged position of the westerly jets. Only a portion of the tracers initialized in each case is shown for clarity of behavior, and approximately 100 timesteps are plotted for each tracer to show the relative movement of the particles. Figures 7 and 8 show the positions of tracers after ten turnover times. In both beta cases, tracers have dispersed into the westerlies, but in the $\beta=.25$ case, at least one

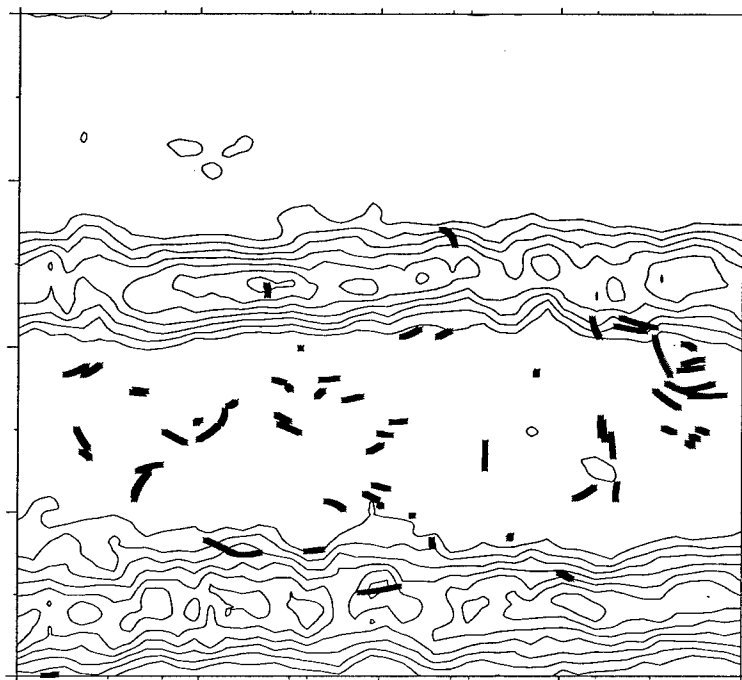


Figure 7 Tracer trajectories for $\beta=0.25$ at $10T_E$.

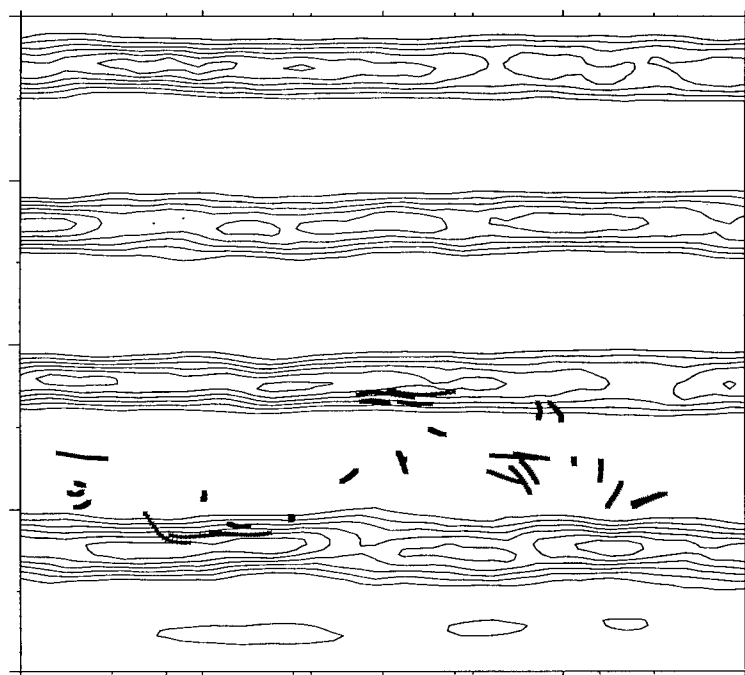


Figure 8 Tracer trajectories for $\beta=0.4$ at $10T_E$.

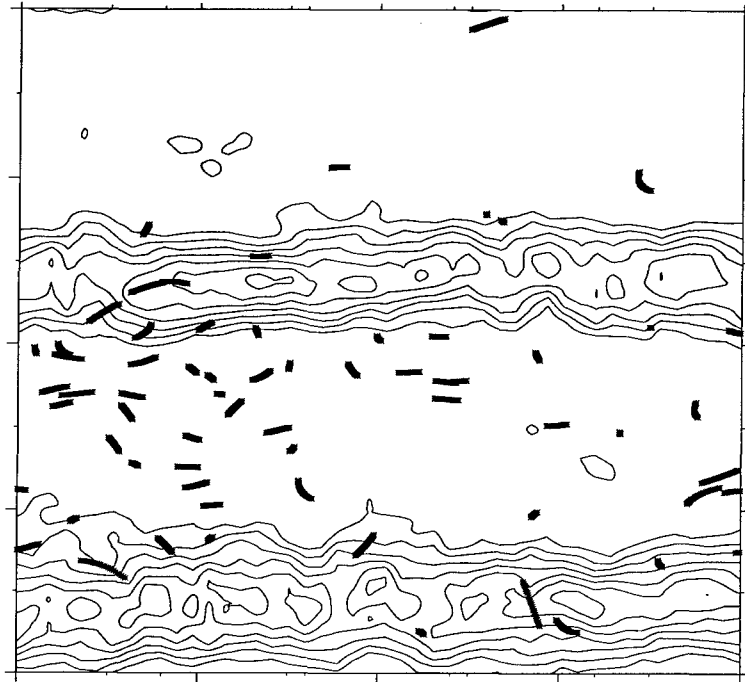


Figure 9 As in figure 7 but for $20T_E$.

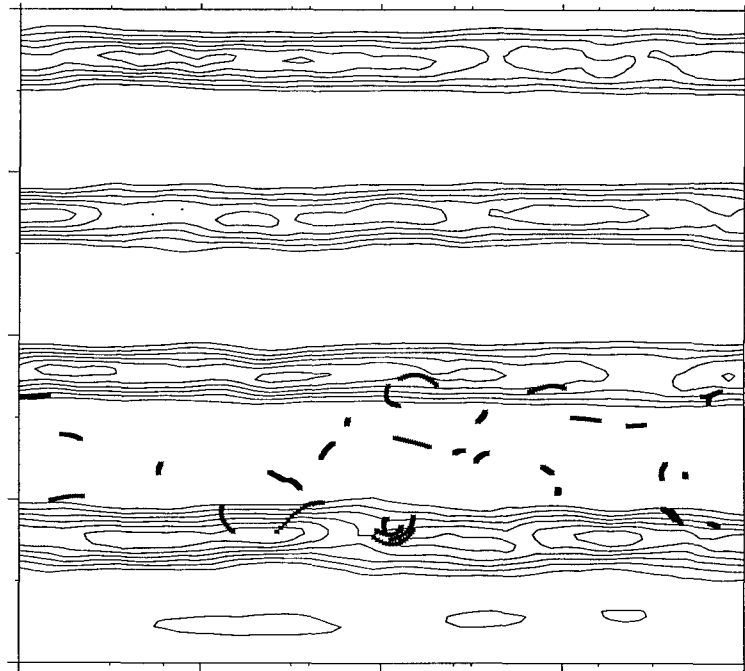


Figure 10 As in figure 8 but for $20T_E$.

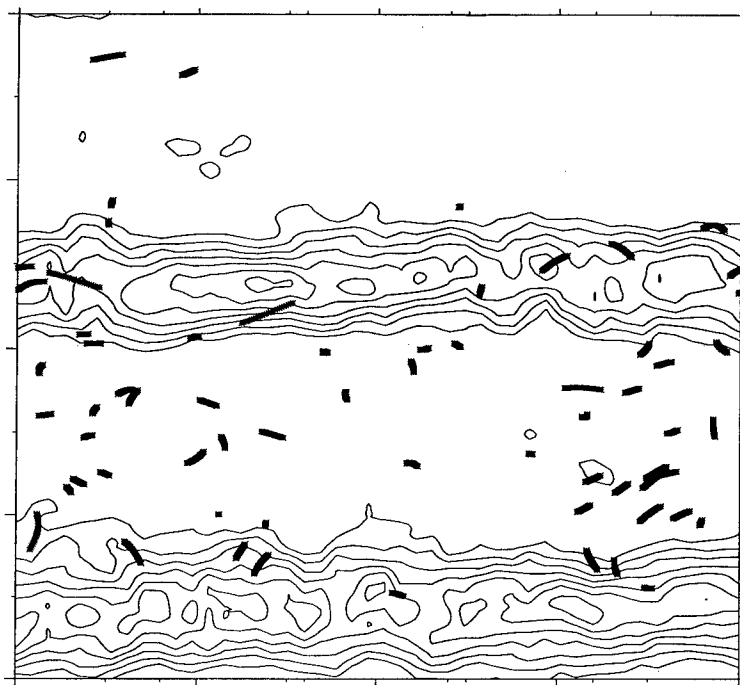


Figure 11 As in figure 7 but for $30T_E$.

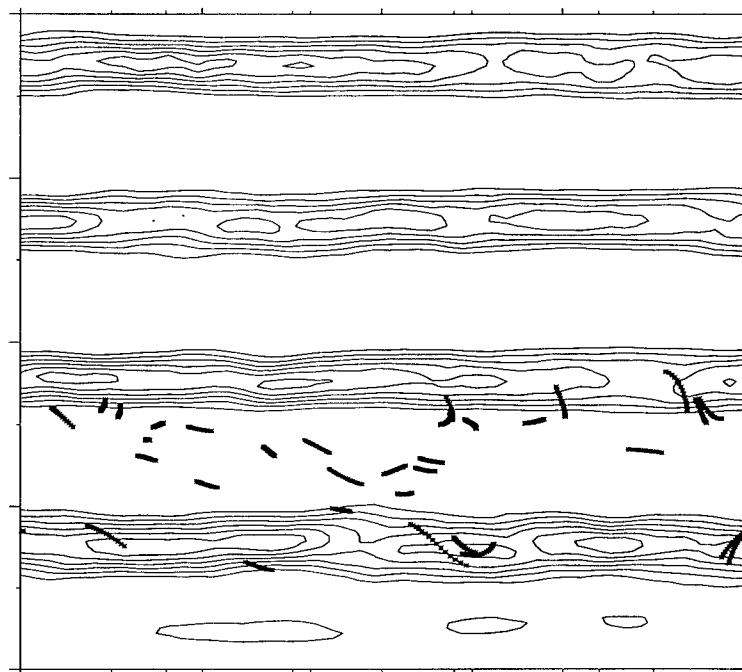


Figure 12 As in figure 8 but for $30T_E$.

tracer has passed through a jet (lower left of figure 7). After $20T_E$ (figures 9 and 10), more tracers have crossed the jets in the low-beta case, while no tracers have done so in the $\beta=.4$ case. Tracers in the high-beta case have thus far been unable to traverse the jet core. Finally, figures 11 and 12 show trajectories after thirty turnover times. Again, in the low-beta case, some tracers have been able to pass through the jets, whereas cross-jet dispersion is still inhibited in the high-beta case. This sequence of figures seems to indicate that, although meridional dispersion is not affected by the value of β , there is clearly something associated with the westerly jets that is β dependent and affects northerly/southerly transport.

Although not reproducible here, animations of the upper-layer potential vorticity fields clearly show that Rossby wave-breaking is enhanced in the low-beta case. Three instantaneous fields from these animations are shown in figures 13-15 for $\beta=.25$, and figures 16-18 for $\beta=.4$. (Note: The low-beta case was done for 128^2 resolution due to time constraints, so the quality of the images in figures 16-18 is degraded compared to the 256^2 images.) The average positions of the maximum gradient in potential vorticity associated with the jet cores of the $\beta=.25$ case are seen at latitudes 20 and 150 (labelled in grid points). The Rossby waves in the low-beta case are extremely distorted due to wave-breaking, and the only part of the maximum p.v. gradient that appears to be stable during this period of the integration is at the right side of the northern jet. The figures for the high-beta case, however, show a reduction

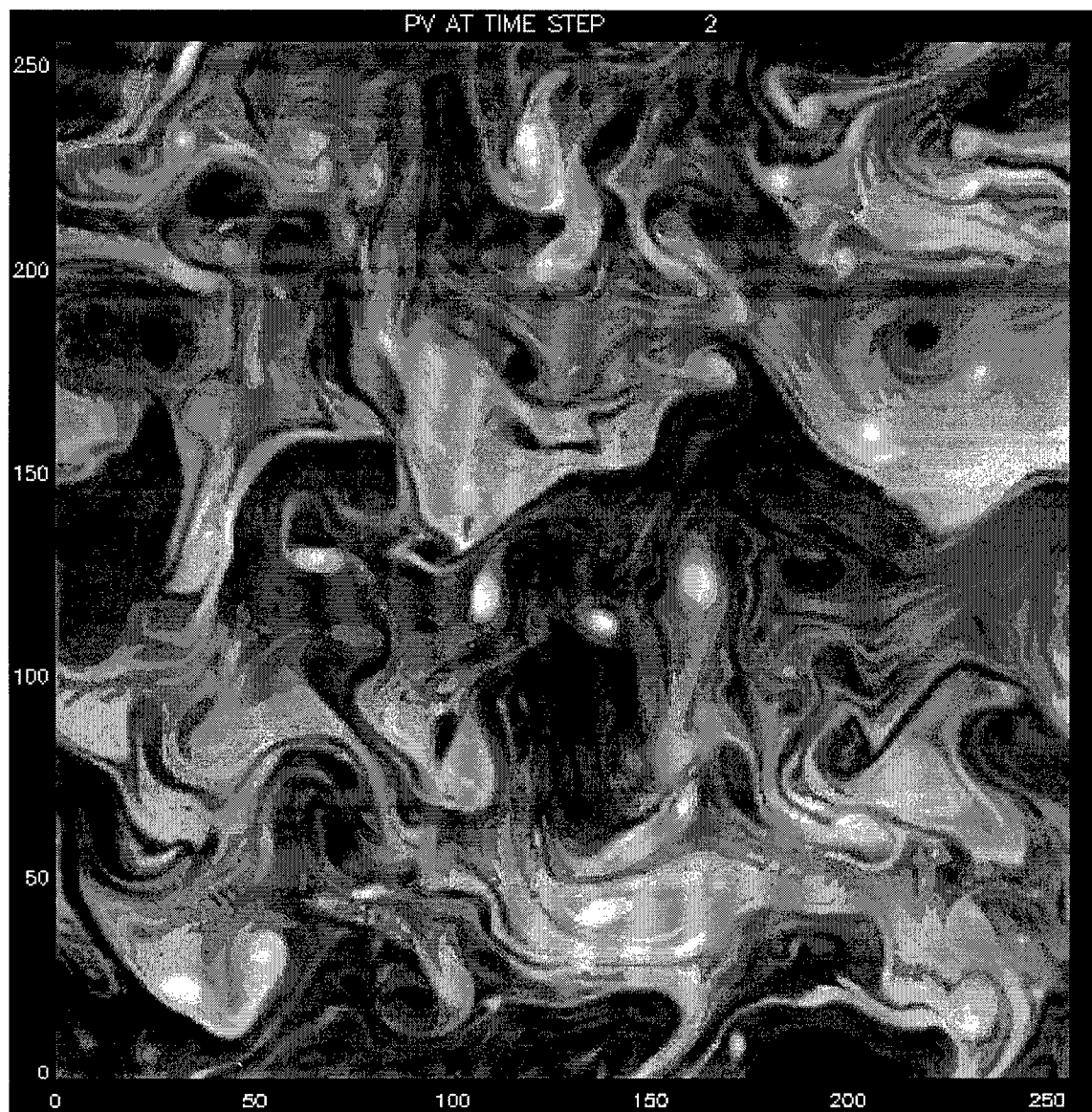


Figure 13 Potential vorticity field for $\beta=.25$ at time step 2.

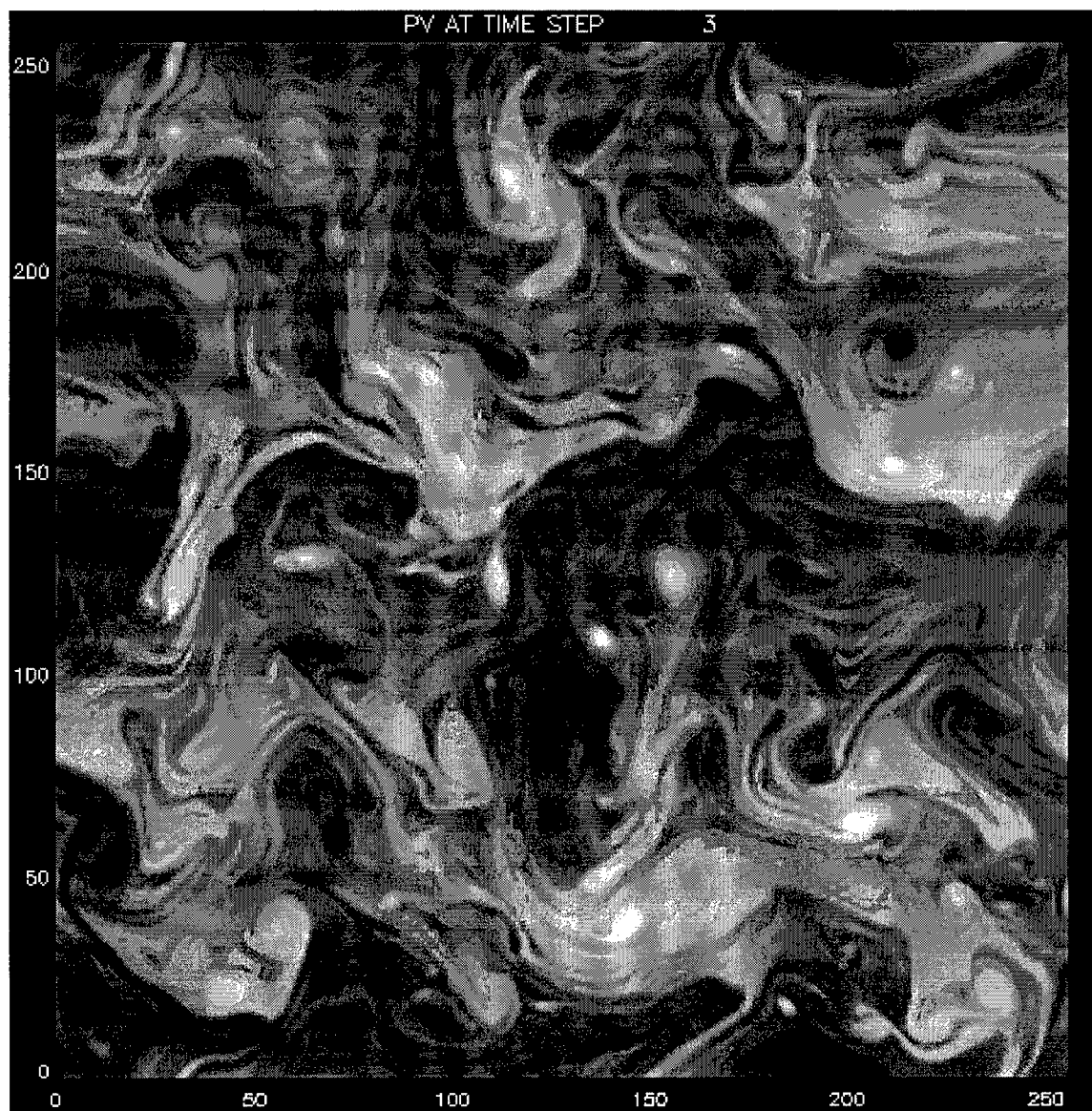


Figure 14 As in figure 13 but for time step 3.

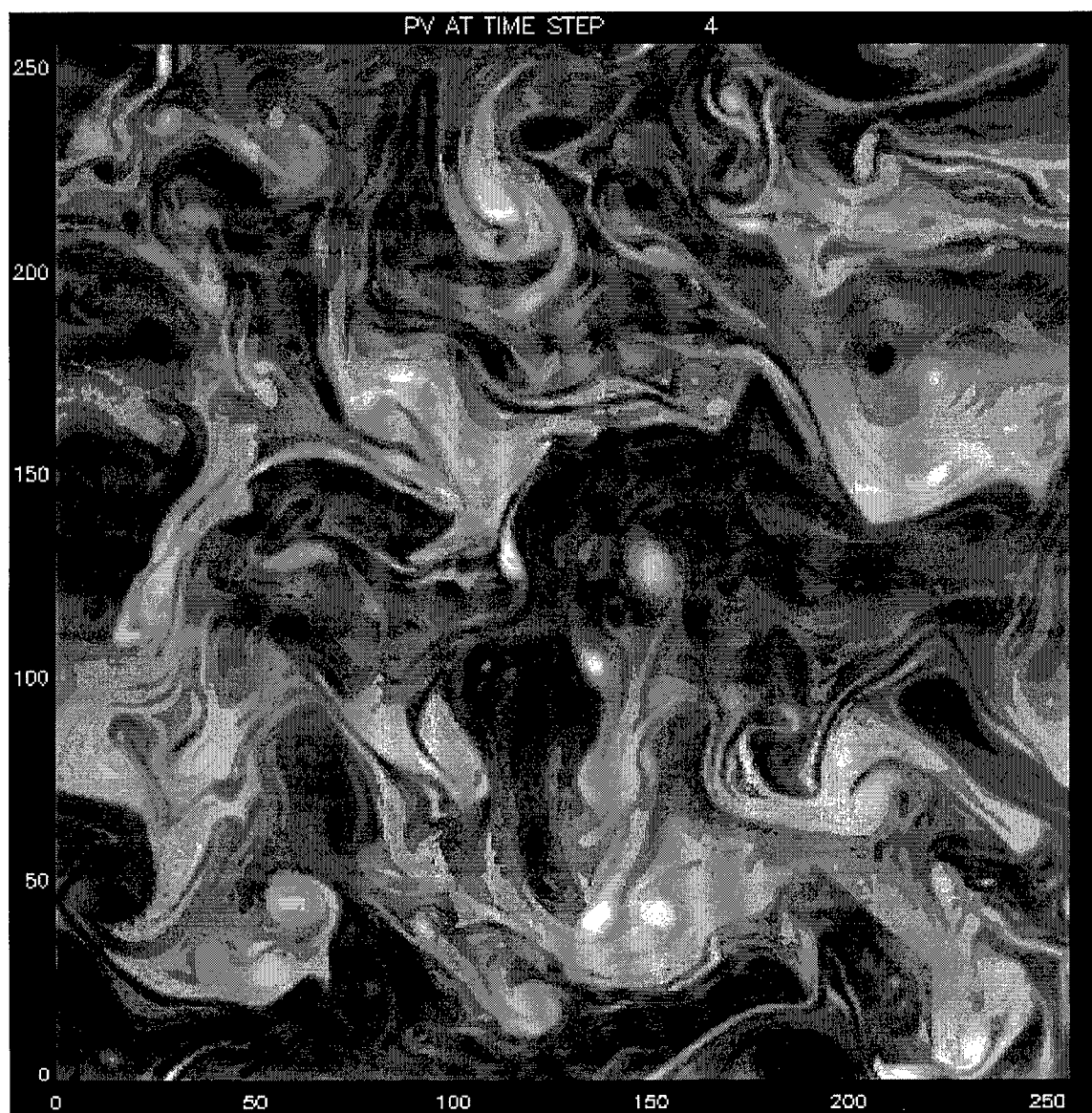


Figure 15 As in figure 13 but for time step 4.

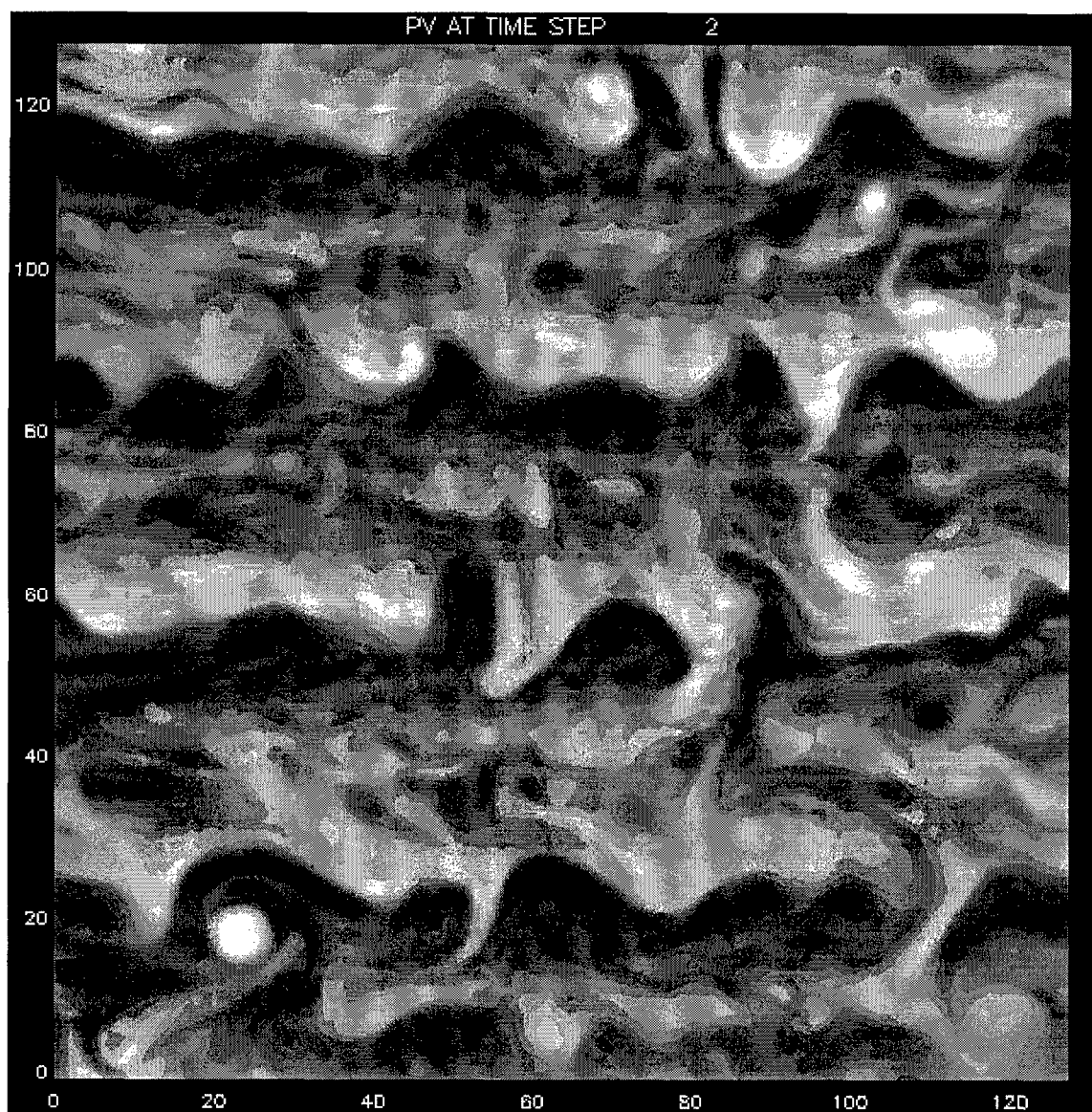


Figure 16 Potential vorticity field for $\beta=.4$ at time step 2.

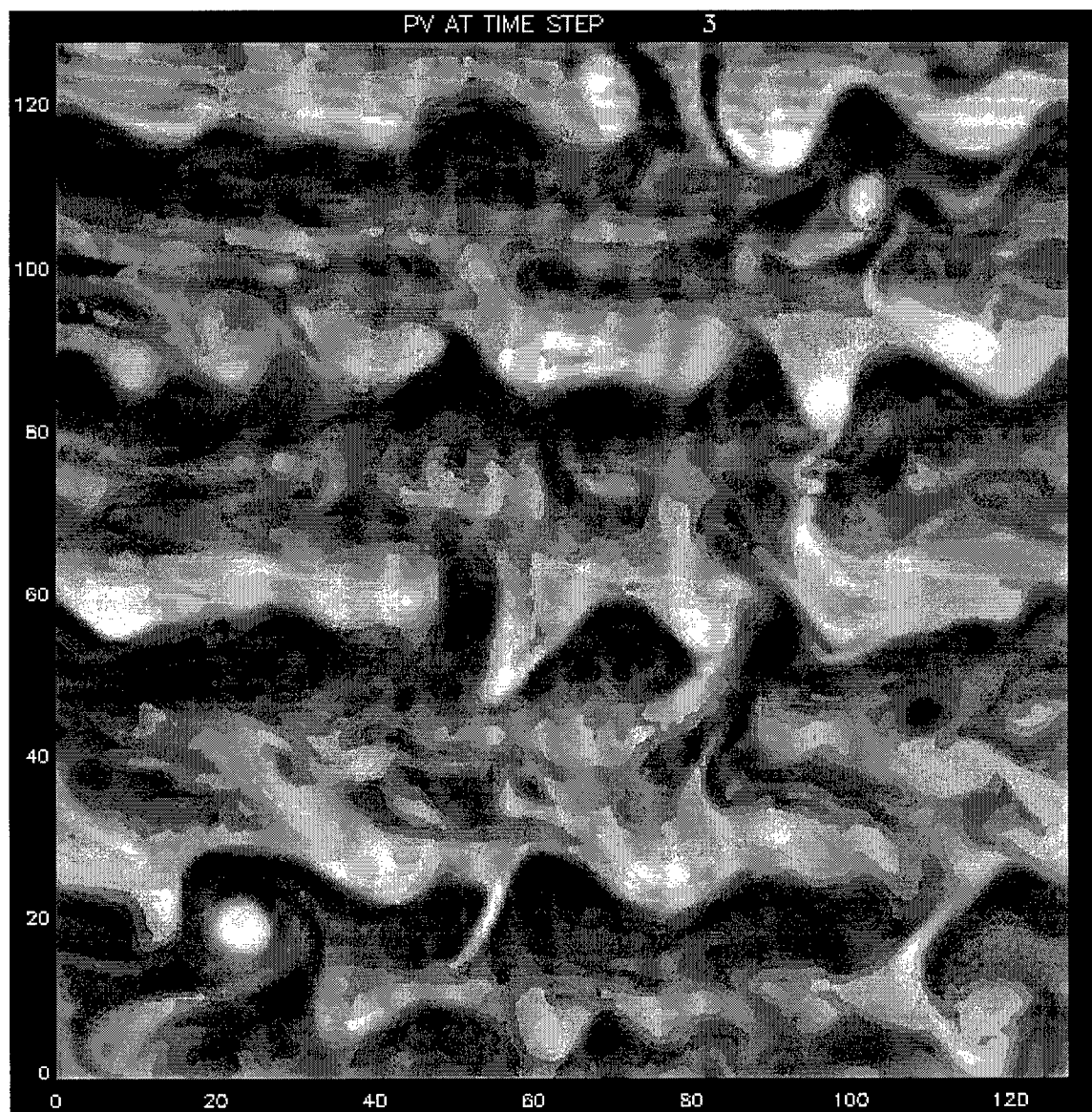


Figure 17 As in figure 16 but for time step 3.

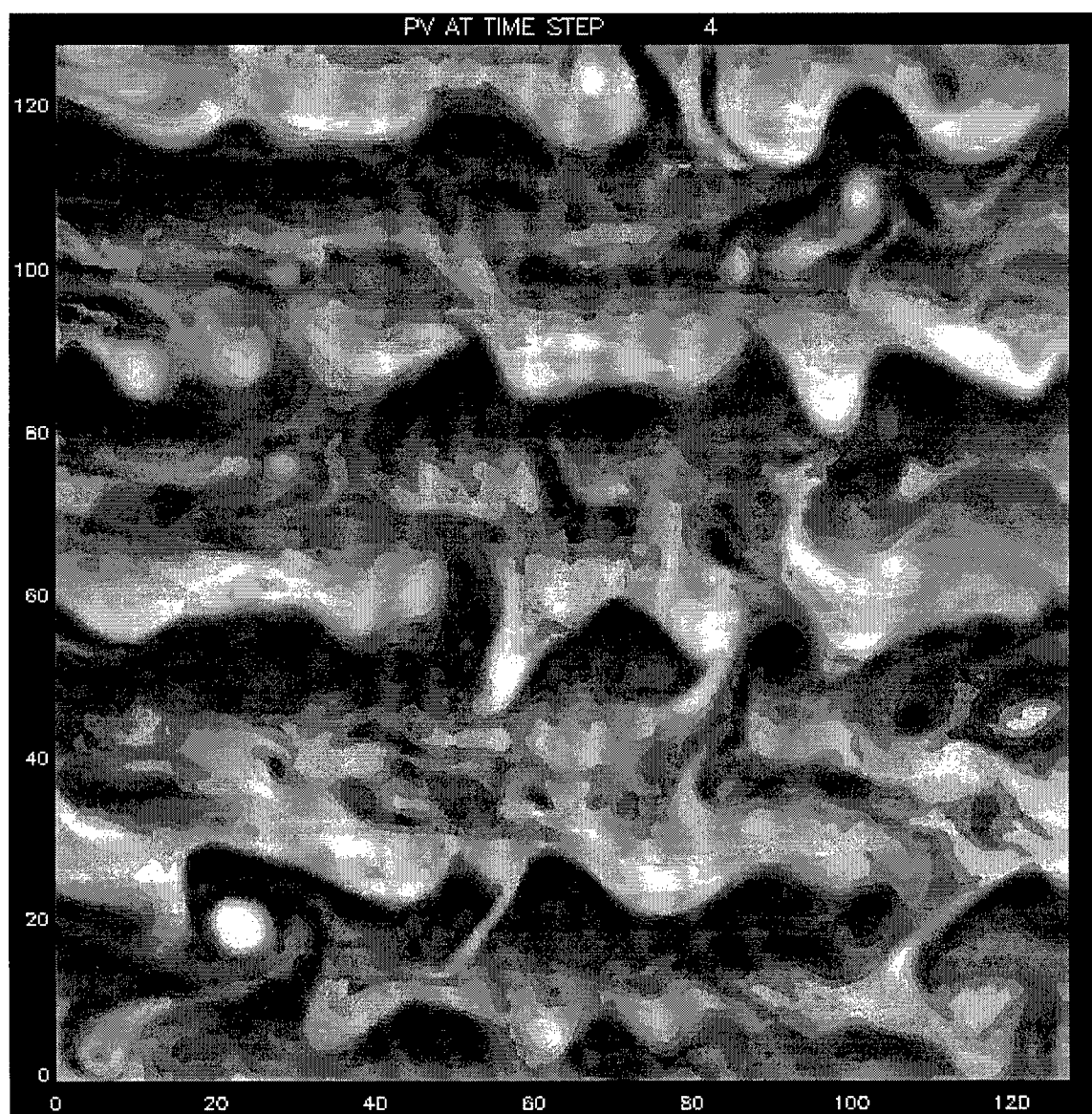


Figure 18 As in figure 16 but for time step 4.

in wave-breaking activity. (The $\beta=.4$ case has four jets, located at grid-point latitudes 20, 55, 88, and 116.) Wave amplitudes are much smaller in this case, and there are several sections along the maximum potential vorticity gradient where waves are extremely weak. While wave-breaking is still present when $\beta=.4$, the frequency of the breaking and the scale of the breaking waves are significantly reduced. Differences in wave-breaking activity between the two beta cases are explainable by the differing energies of the flows. The total energy in the $\beta=.25$ case is 8.6 (nondimensional units of U_o^2), and the $\beta=.4$ case has a total energy of 1.5 units. The fact that the rescaling of time in each beta case, based upon differences in *eddy* energies, resulted in comparable meridional dispersions indicates that most of the eddy energy in each system is contained within the easterlies. The amount of *total* energy in the flow does, however, affect the westerlies, and translates into increased wave-breaking in the low-beta case. This results in a difference in tracer transport across the jets in the two systems.

Thus, it has been shown that an increase in the planetary vorticity gradient enhances zonal dispersion and has no effect on meridional dispersion in regions away from wave-breaking, and increases meridional dispersion near the westerly jet core. These results rely upon a rescaling of the time and length scales in each beta case to account for differences in energy and number of jets.

Scale Sensitivity

The second objective of this research was to examine the sensitivity of tracer transport to the scales of waves included in the flow field. This was done using the system described in table 2. Contributions from unwanted wavenumbers were removed from the background flow before advecting the tracers by multiplying the velocity vectors in wavenumber space by 1.0 if $K \leq K_{co}$ and by 0.0 if $K > K_{co}$. The cutoff wavenumber, K_{co} , was assigned a different value for each of the four cases to be examined: $K_{co} = 60$ (i.e., no waves removed), 20, 10 and 5. These wavenumbers correspond to 4λ , 1.3λ , $.6\lambda$, and $.3\lambda$ respectively, where λ is the Rossby radius of deformation.

Figures 19-22 show the effect of wavenumber removal on the eddy potential vorticity field in the upper layer. The graphs show the upper layer p.v. fields in which the tracers were initialized, for the range of K_{co} values. As the number of waves truncated increases (figures 20-22), small-scale effects on the flow disappear, and the p.v. fields become greatly smoothed. (Note: for clarity of the image, the contour interval used in figure 19 is twice that used in figures 20-22.) The potential vorticity gradient decreases in the jet core region, and the jets become increasingly

Table 2 Parameters used in scale sensitivity simulations.

<i>Resol.</i>	\hat{L}	β	κ_M	ν
128^2	15	.20	.05	$3.E10^{-5}$

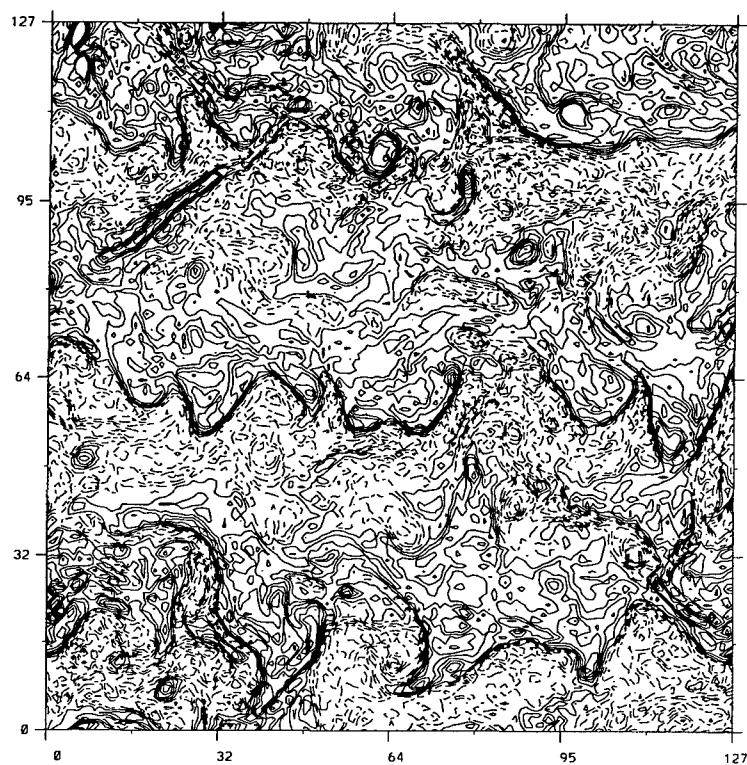


Figure 19 Initial potential vorticity field for $K_{co} = 60$.

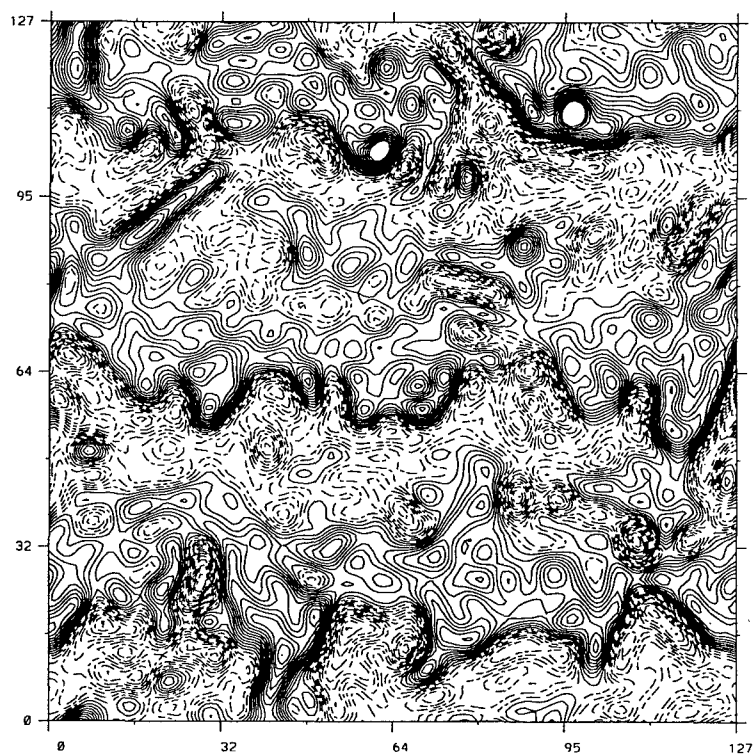


Figure 20 As in figure 19 but for $K_{co} = 20$.

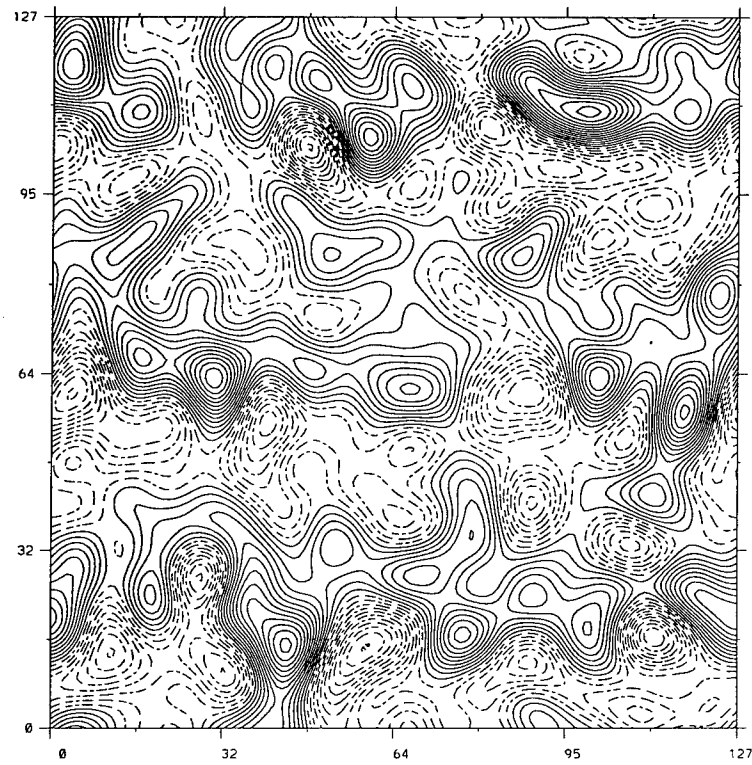


Figure 21 As in figure 19 but for $K_{co} = 10$.

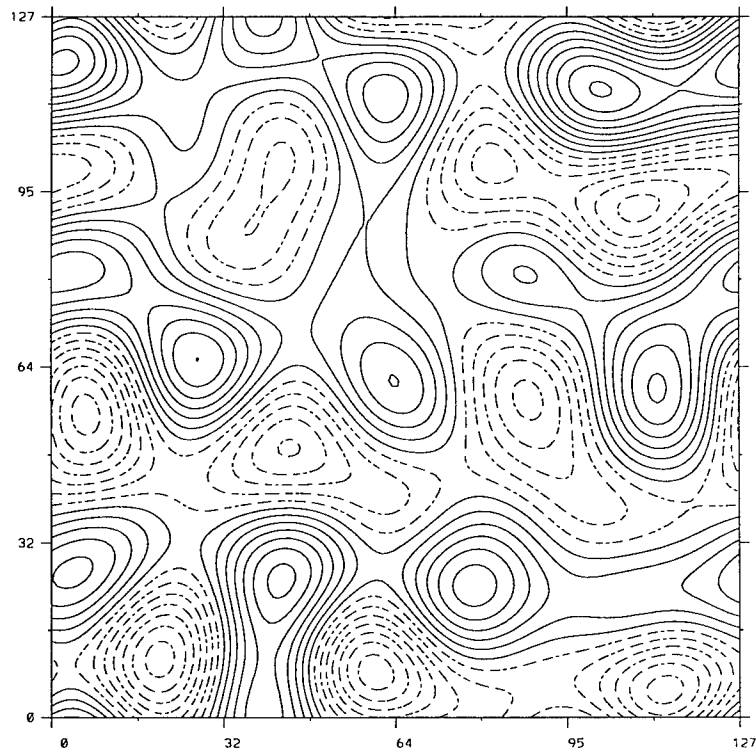


Figure 22 As in figure 19 but for $K_{co} = 5$.

difficult to pinpoint, particularly when $K_{co} < 10$ (figure 22).

In these scale sensitivity simulations, tracers were initialized in the easterlies only, so that tracer behavior in and around the maximum potential vorticity gradient associated with the westerly jet core could be easily distinguished. In other words, if tracer statistics representing meridional dispersion exhibit a *decrease* of displacement in time, we may conclude that tracers are experiencing some barrier to dispersion as they spread out from the easterlies.

Figures 23-26 show the ensemble average single-particle, or rms, displacements as a function of time for the four K_{co} values. In each plot, zonal rms displacement is given by curve A, meridional displacement by curve B. Although there are very slight differences in the slopes of the zonal curves in the four cases, the east/west dispersion in each may be characterized by an initial period of super-linear dispersion lasting only a few timesteps, and a period of a few days in which dispersion occurs at a rate proportional to T . Tracers spend the majority of their time, however, dispersing at a rate slightly less than linear, though certainly not approaching the \sqrt{T} behavior expected in isotropic, homogeneous turbulence. As K_{co} decreases, the long-term behavior of particle dispersion seems to more closely resemble linear growth, although the slope of the rms displacement curve is still slightly less than 1.0. This would imply that tracer trajectories in the $K_{co}=5$ case are more zonally oriented than those in the $K_{co}=60$ case. In fact, after 50 nondimensional days, a tracer would have

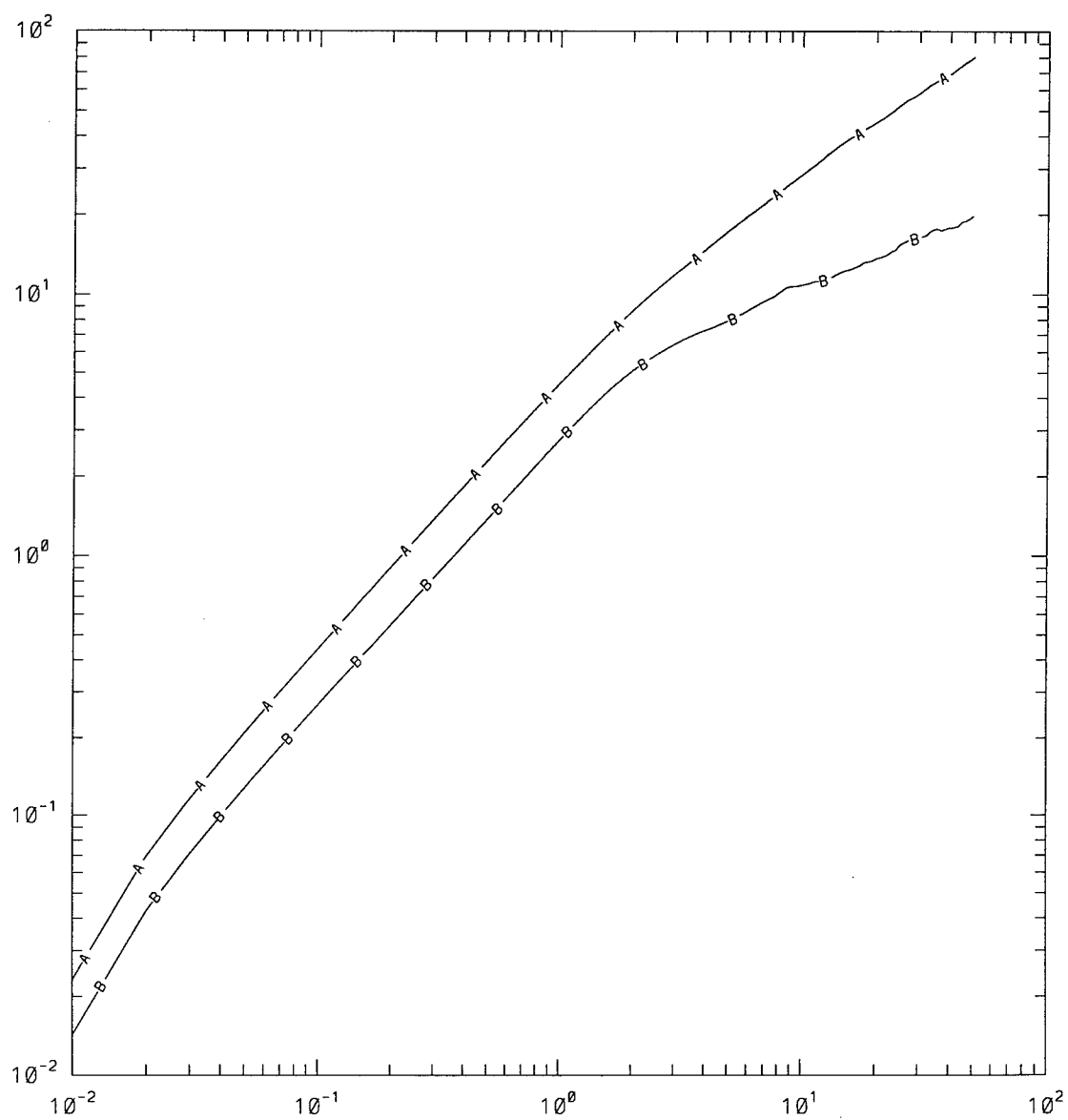


Figure 23 Single-particle displacements for $K_{co}=60$. Log of displacement in λ on ordinate, log of nondimensional time on abscissa. Curve A is zonal displacements, curve B is meridional displacements.

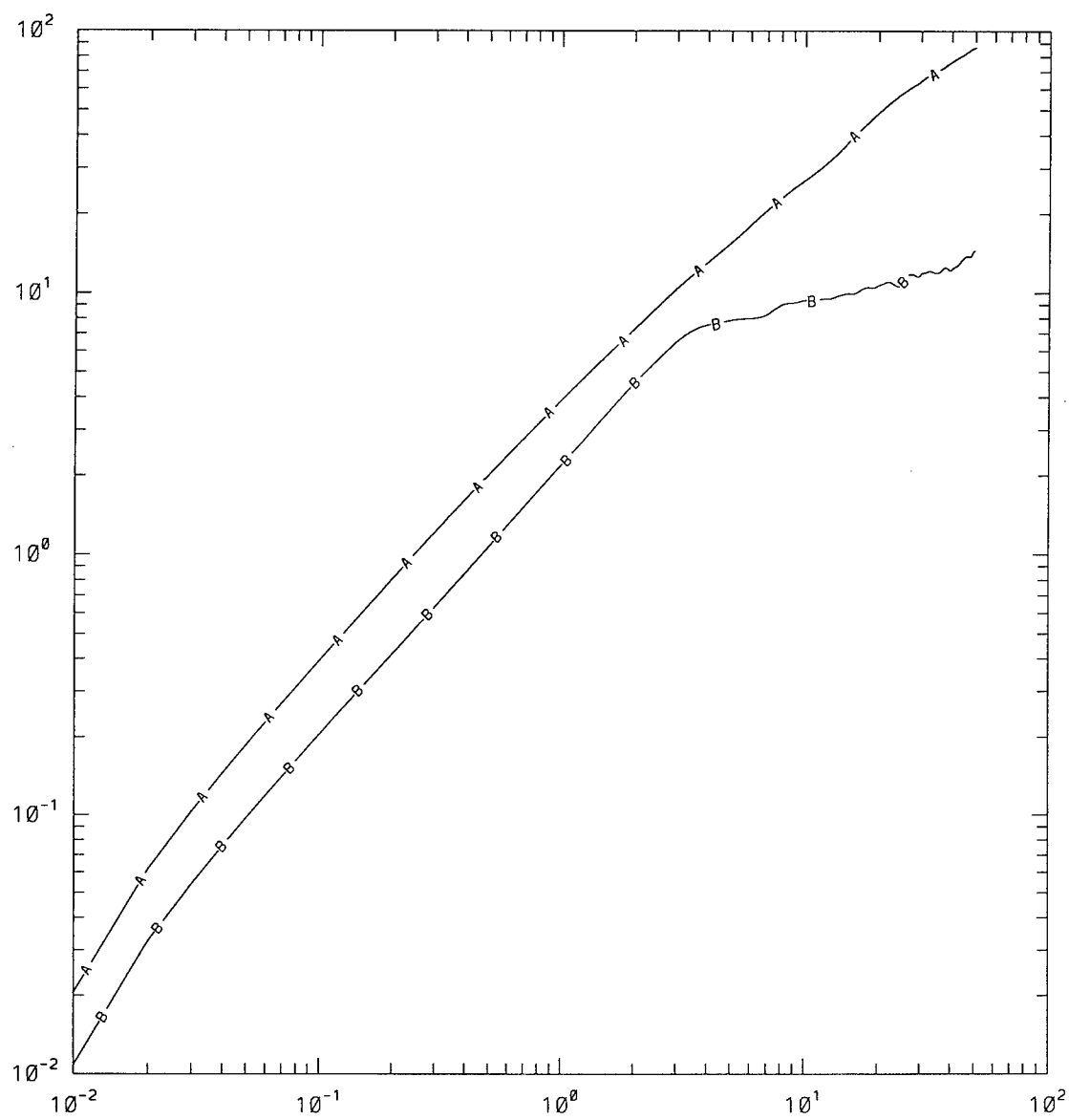


Figure 24 As in figure 23 but for $K_{co} = 20$.

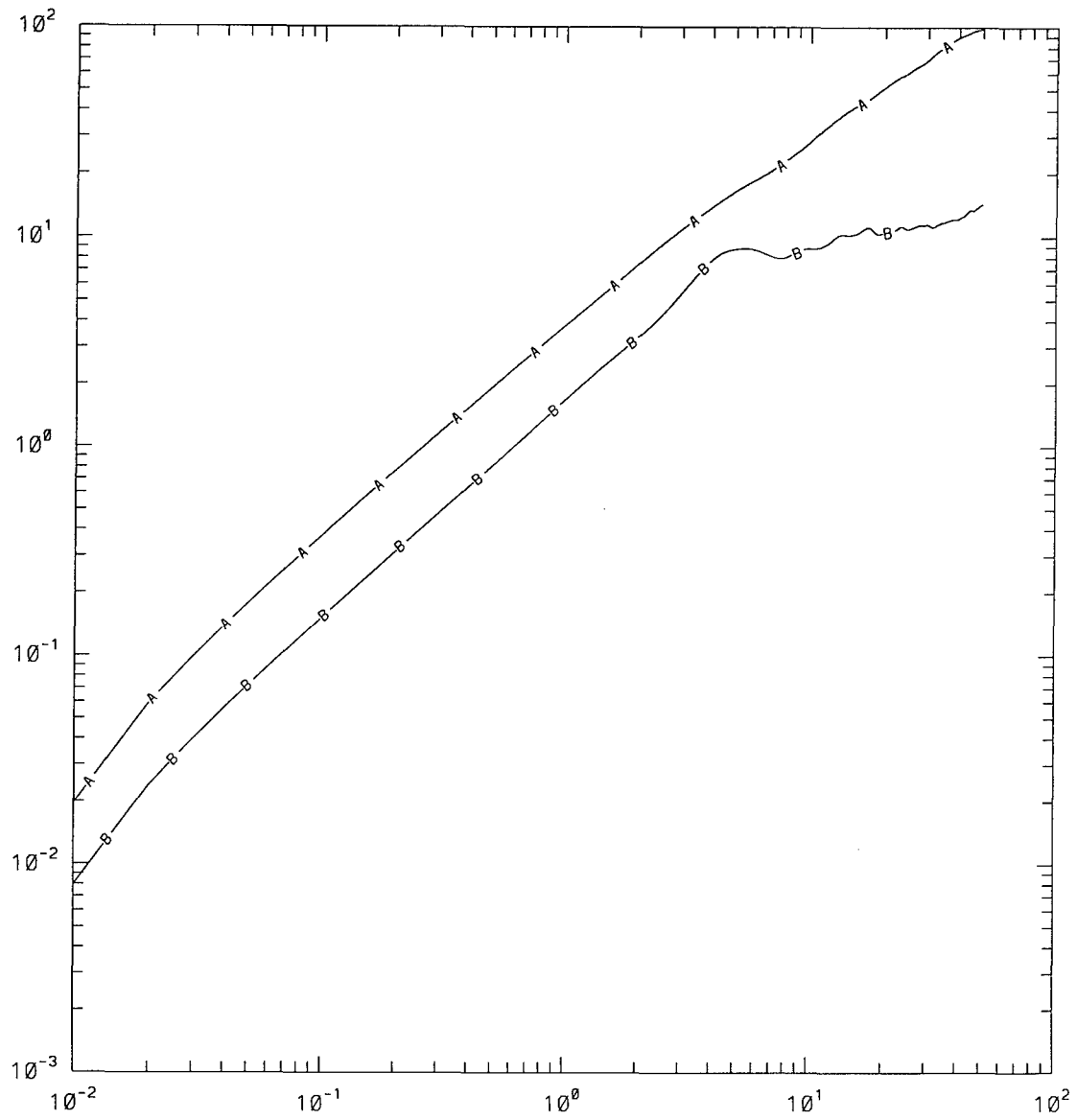


Figure 25 As in figure 23 but for $K_{co} = 10$.

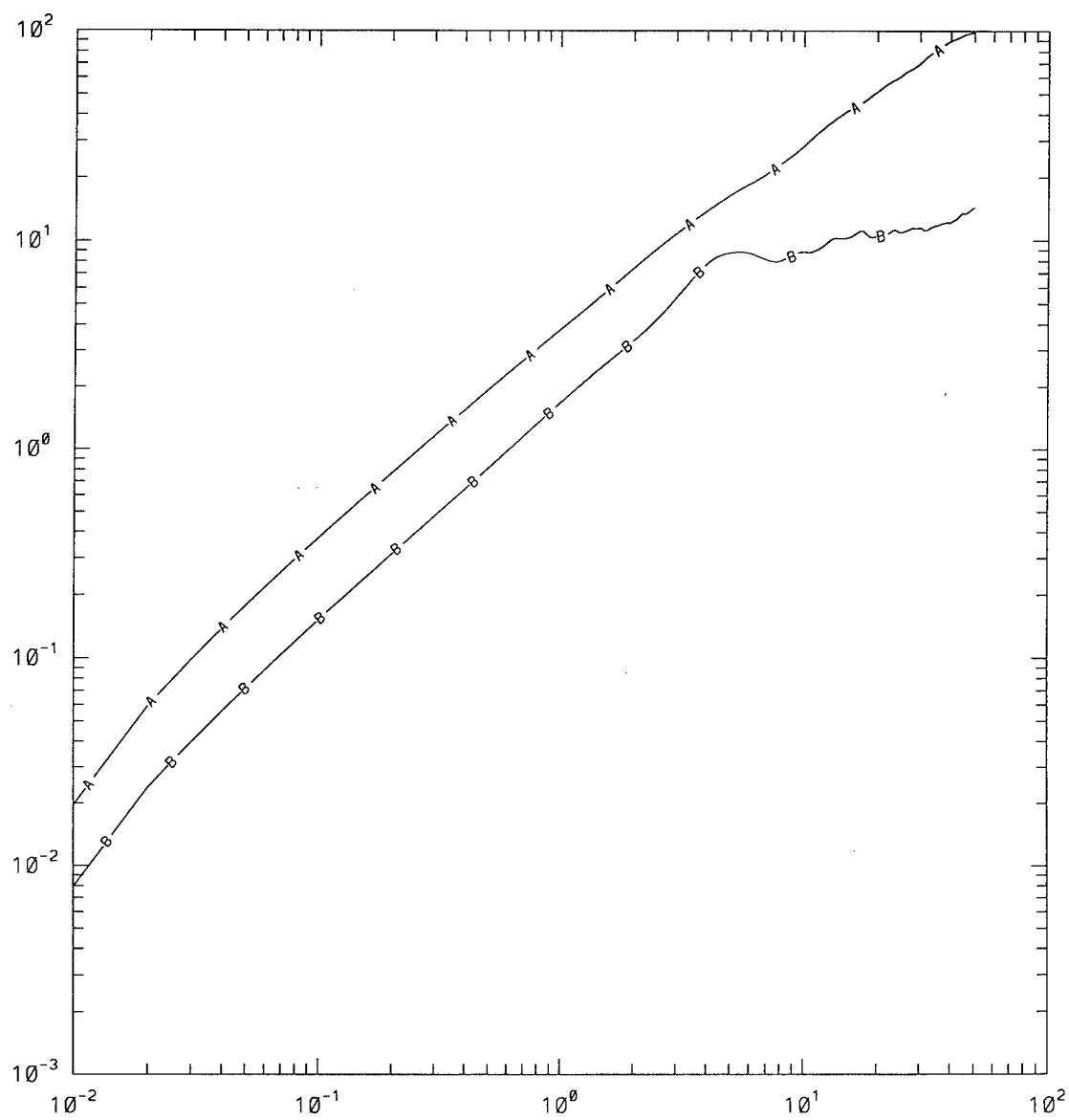


Figure 26 As in figure 23 but for $K_{co} = 5$.

been displaced an average of 80, 88, 100, and (again) 100 Rossby radii for $K_{co}=60, 20, 10$ and 5, respectively. It seems that small scales act to inhibit zonal single-particle displacements.

When considering meridional rms displacements, however, the result is just the opposite. Tracers initialized in the full wavenumber case were displaced an average of 20λ by the end of the integration, while tracers in the other three cases were only displaced 14λ in the same period. A qualitative comparison of curves B in each of the cases indicates that as the smallest-scale waves are removed from the flow, the rate at which tracers disperse to the north/south decreases for the majority of the time of integration. Unlike Haidvogel's system in which small scales had no effect on single-particle displacements, it appears that in this model, the small scale waves act to increase meridional dispersion, while hindering zonal displacements. This behavior suggests a mechanism, which is enhanced by the presence of small scales, that forces tracers across jets rather than along them.

Figures 27-30 show the two-particle displacements for the four cases. Curve A is for the upper layer in these figures, and curve B is for the lower layer. The total average displacement of pairs of particles after the 50 days of integration does show a dependence on the value of K_{co} . For $K_{co} = 60, 20, 10$ and 5, pairs of particles separate distance of 105, 115, 118 and λ . This statistic only examines the magnitude of particle spreading, not the orientation, so nothing can be said about the direction

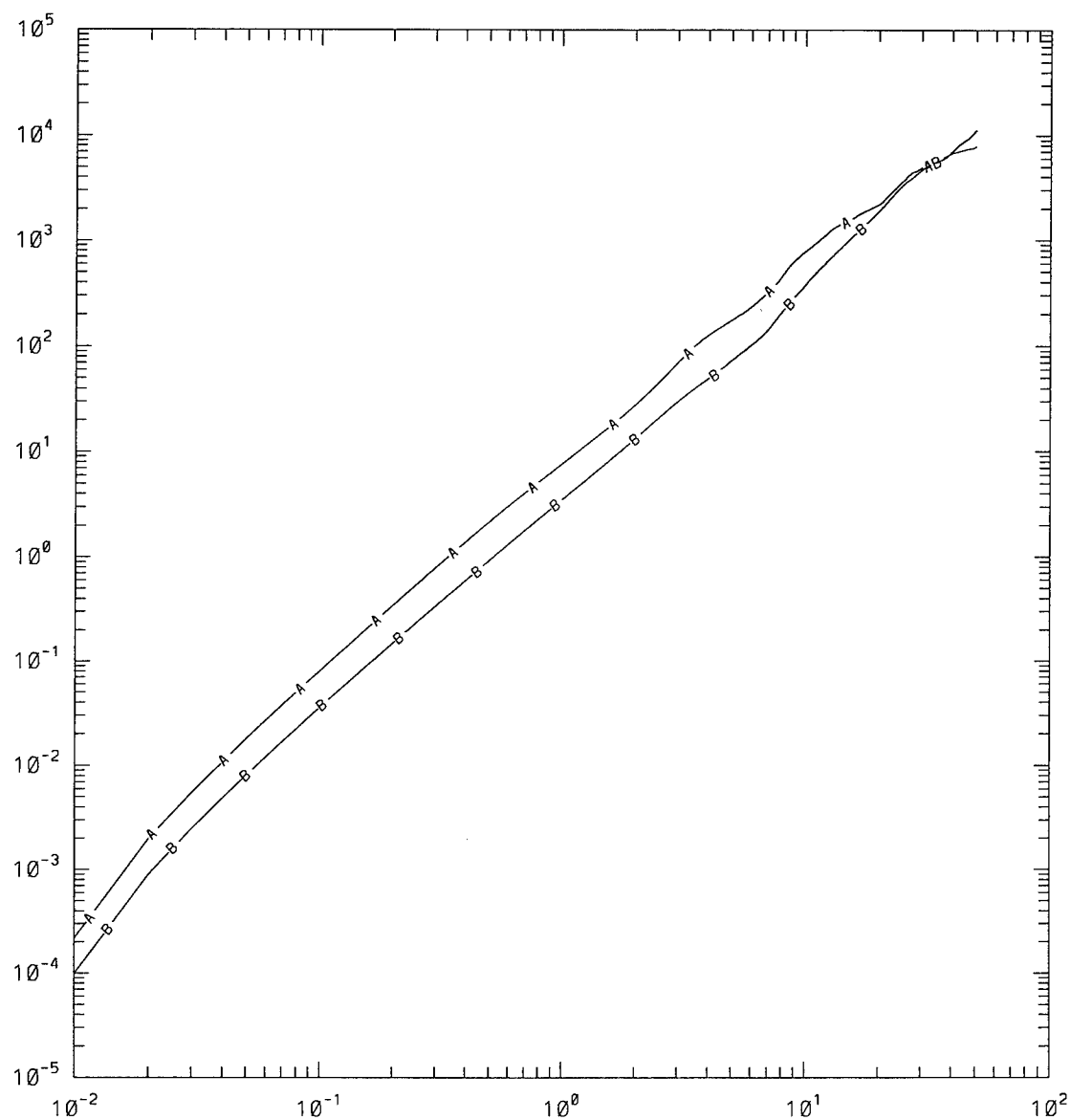


Figure 27 Two-particle displacements for $K_{co}=60$. Log of displacement squared in λ on ordinate, log of nondimensional time on abscissa. Curve A is upper-layer displacements, curve B is lower-layer displacements.

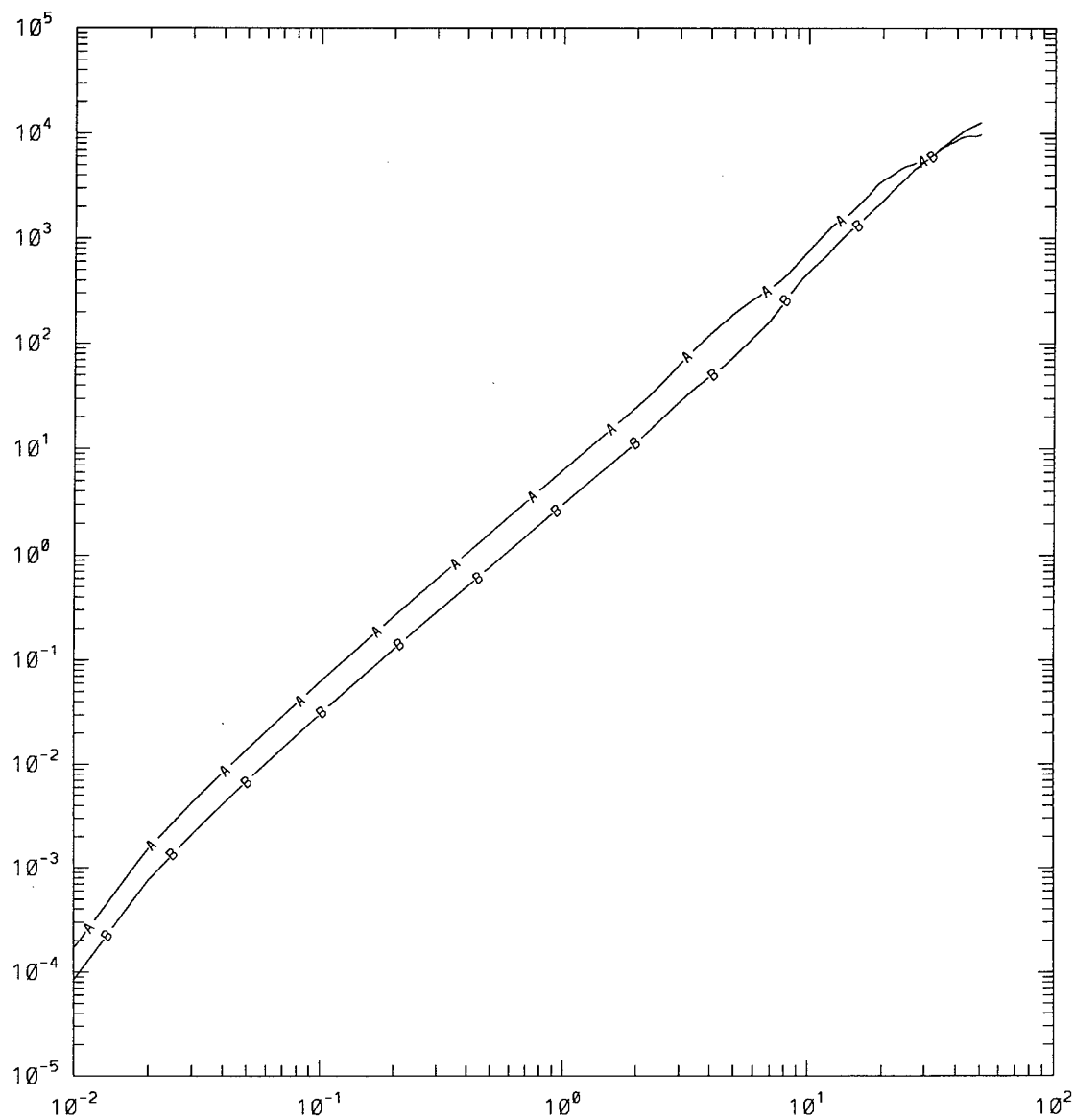


Figure 28 As in figure 27 but for $K_{co} = 20$.

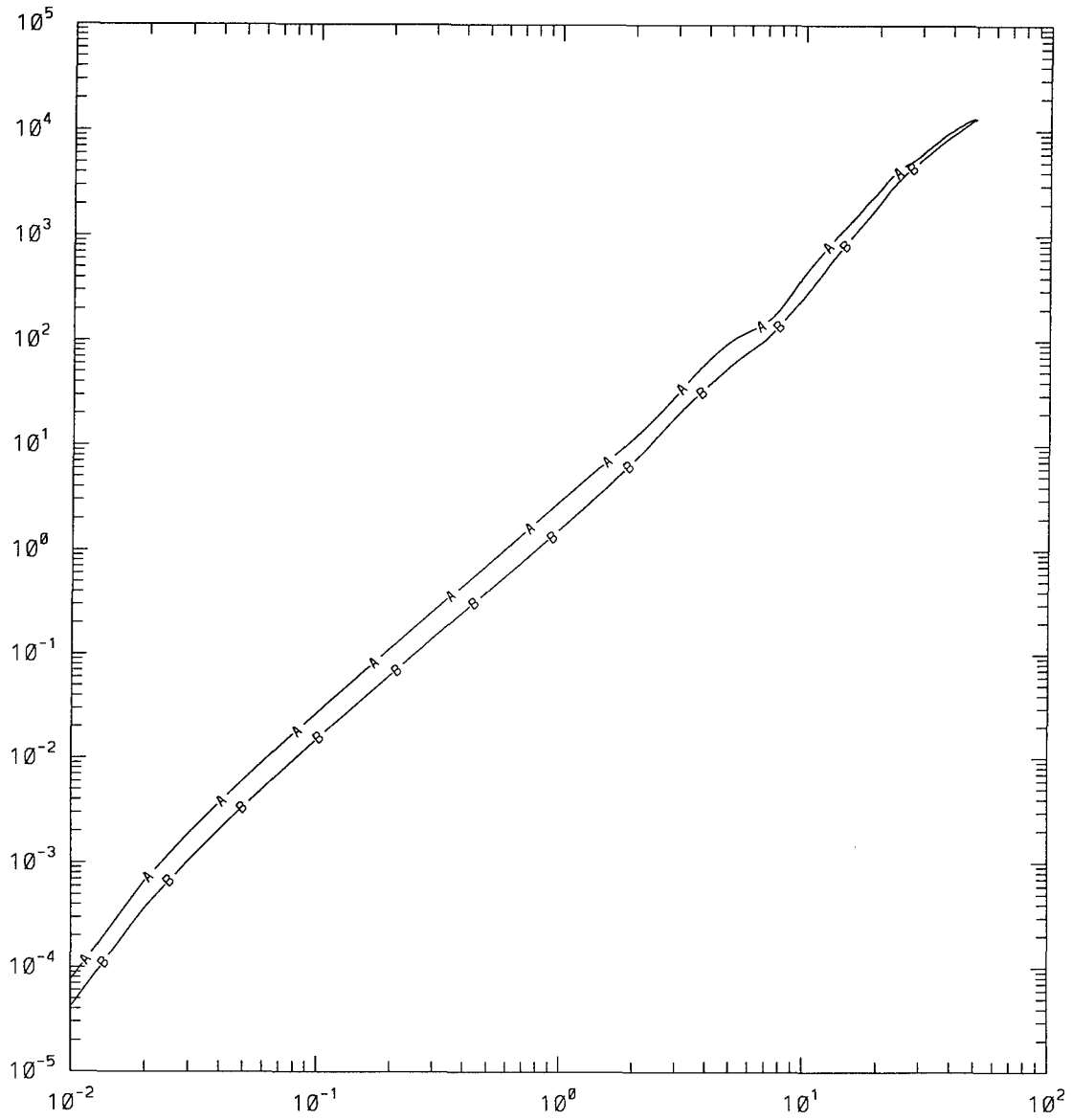


Figure 29 As in figure 27 but for $K_{co} = 10$.

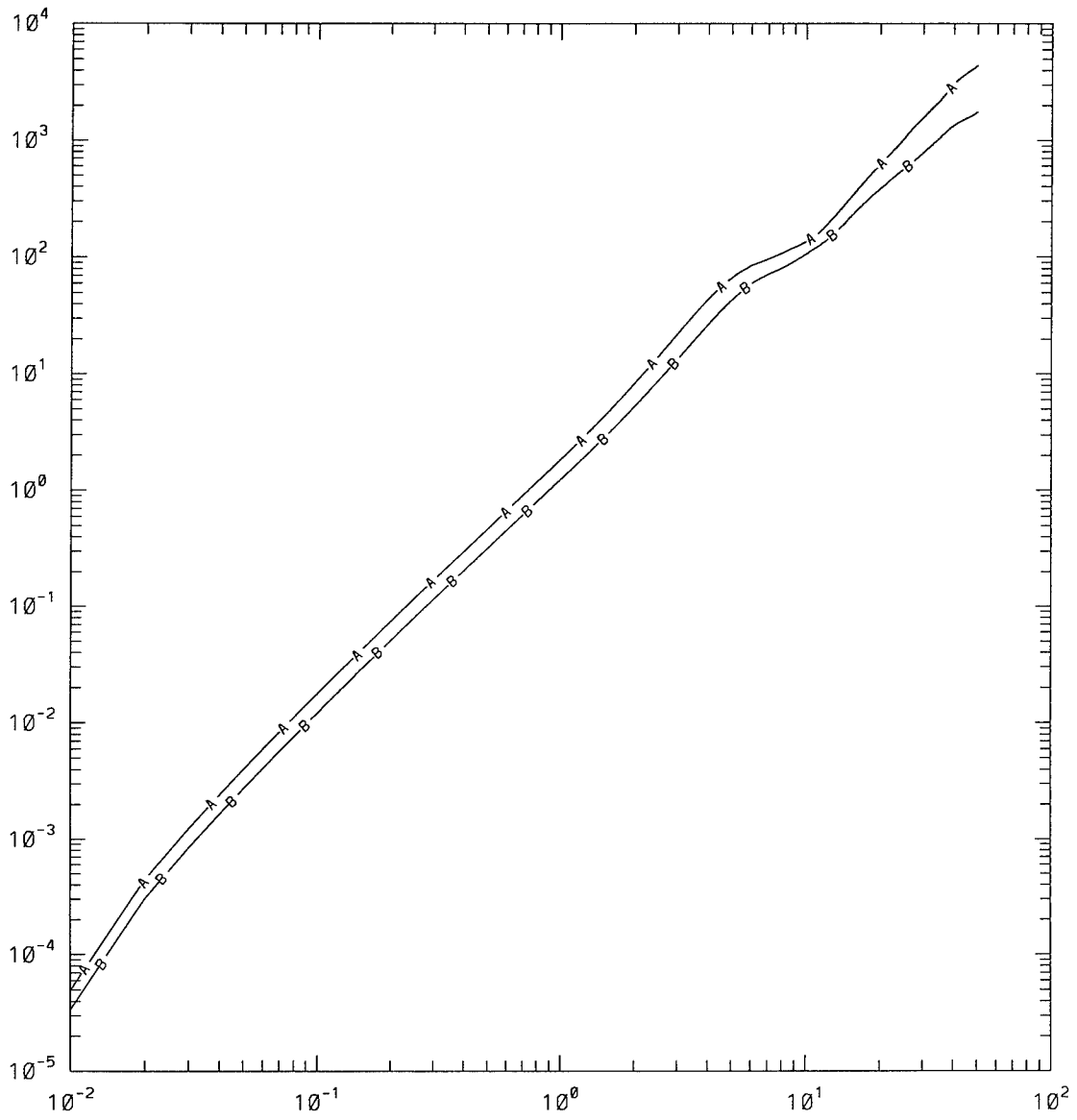


Figure 30 As in figure 27 but for $K_{co} = 5$.

of particle displacements. Since the particle spreading rate is controlled by the shear of the flow rather than the flow velocity, this suggests that inclusion of contributions to the shear by small scale waves are necessary to accurately portray the nature of two-particle spreading. Thus, while Haidvogel found that smoothing of the velocity fields did not affect two-particle statistics, results from this model indicate that small scales do contribute substantially to the flow shear.

The decrease in meridional dispersion, seen in the rms displacements, as the cutoff wavenumber dropped from greater than or equal to 10 to less than 10 is also reflected in the maximum north/south excursion experienced by any particle in each simulation. Figures 31-34 show these maximum excursions for the first 30 days of each case, with solid lines representing the greatest northward distance travelled by any particle, and the dashed lines representing the same for southward movement. For the cases with $K_{co} \geq 10$, there is no indication of any barrier to meridional movement, although the rate of increase of maximum excursion decreases slightly as more waves are removed from the flow. The difference in maximum excursion between the $K_{co}=60$ and $K_{co}=20$ case is approximately 2λ , or $3\Delta x$, where Δx is the space between grid points. Thus, removal of wavenumbers larger than 10 has a slight effect on meridional dispersion. In the $K_{co}=5$ simulation, however, there is clearly some mechanism that acts to minimize meridional transport, so that by the end of the integration, tracers in this case have dispersed only half the distance of tracers in the $K_{co}=60$ case.

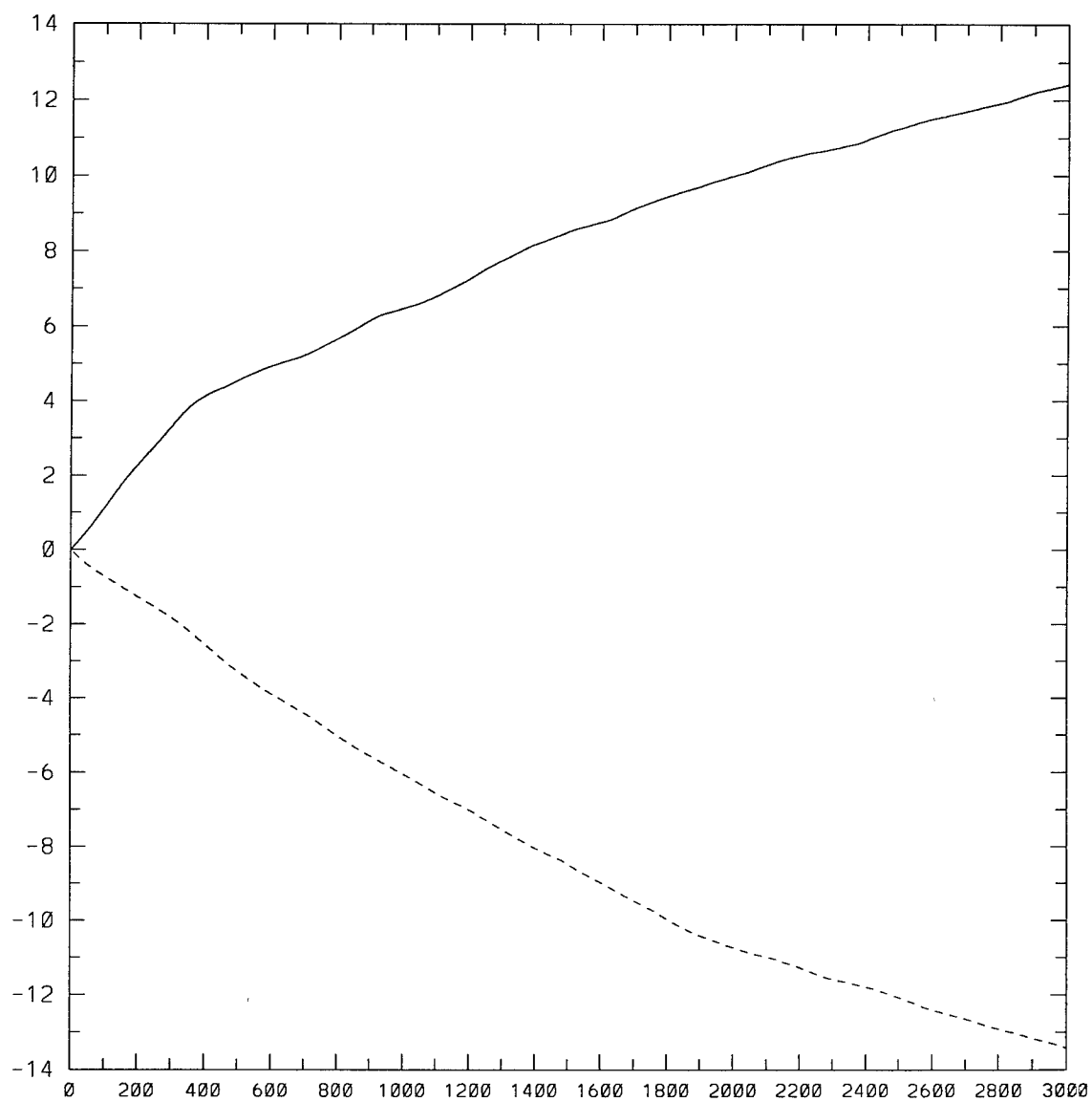


Figure 31 Maximum meridional excursions for $K_{co}=60$. Maximum displacement in λ on ordinate, timesteps on abscissa. Solid line indicates northerly excursions, dashed line indicates southerly excursions.

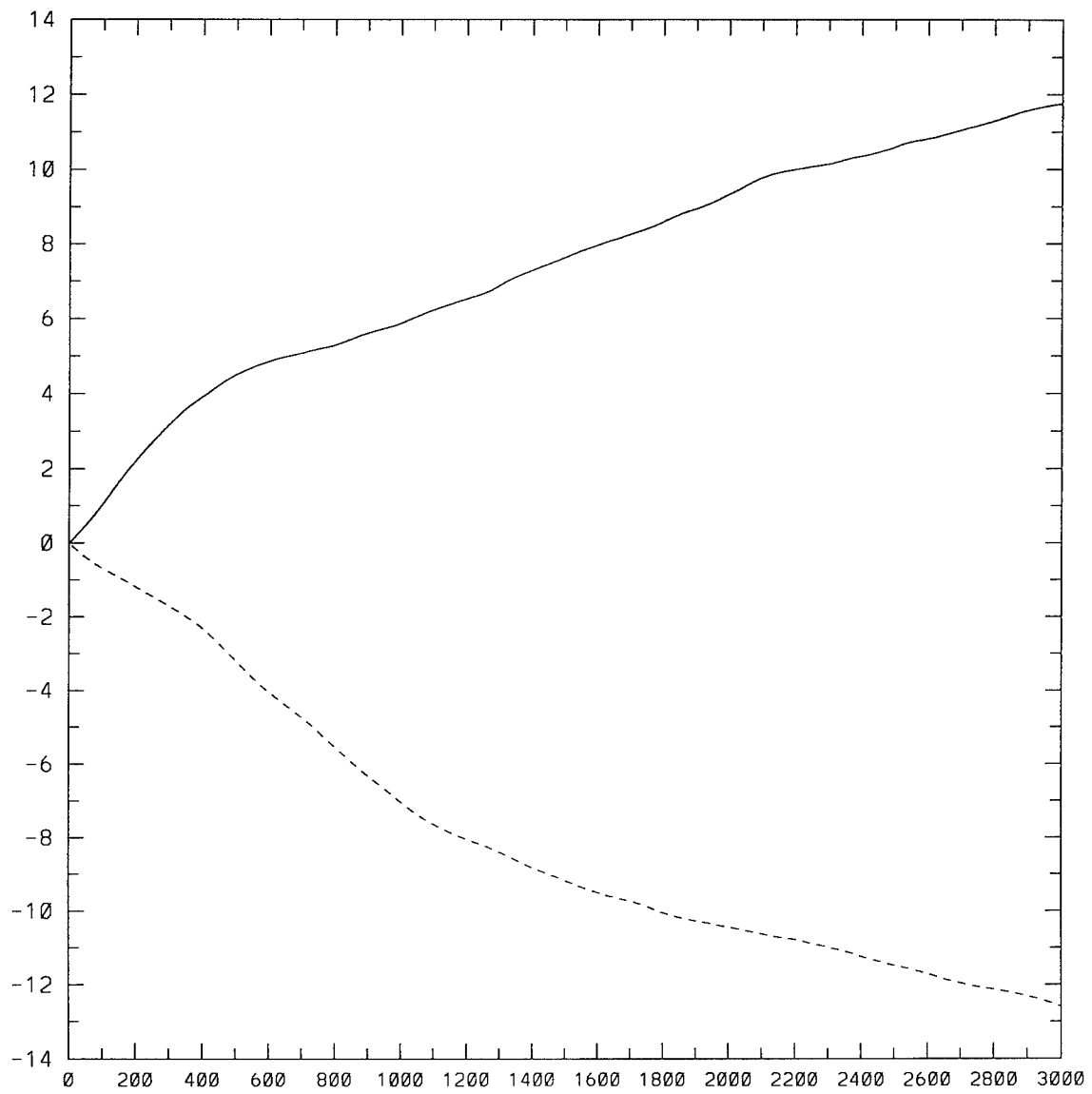


Figure 32 As in figure 31 but for $K_{co} = 20$.

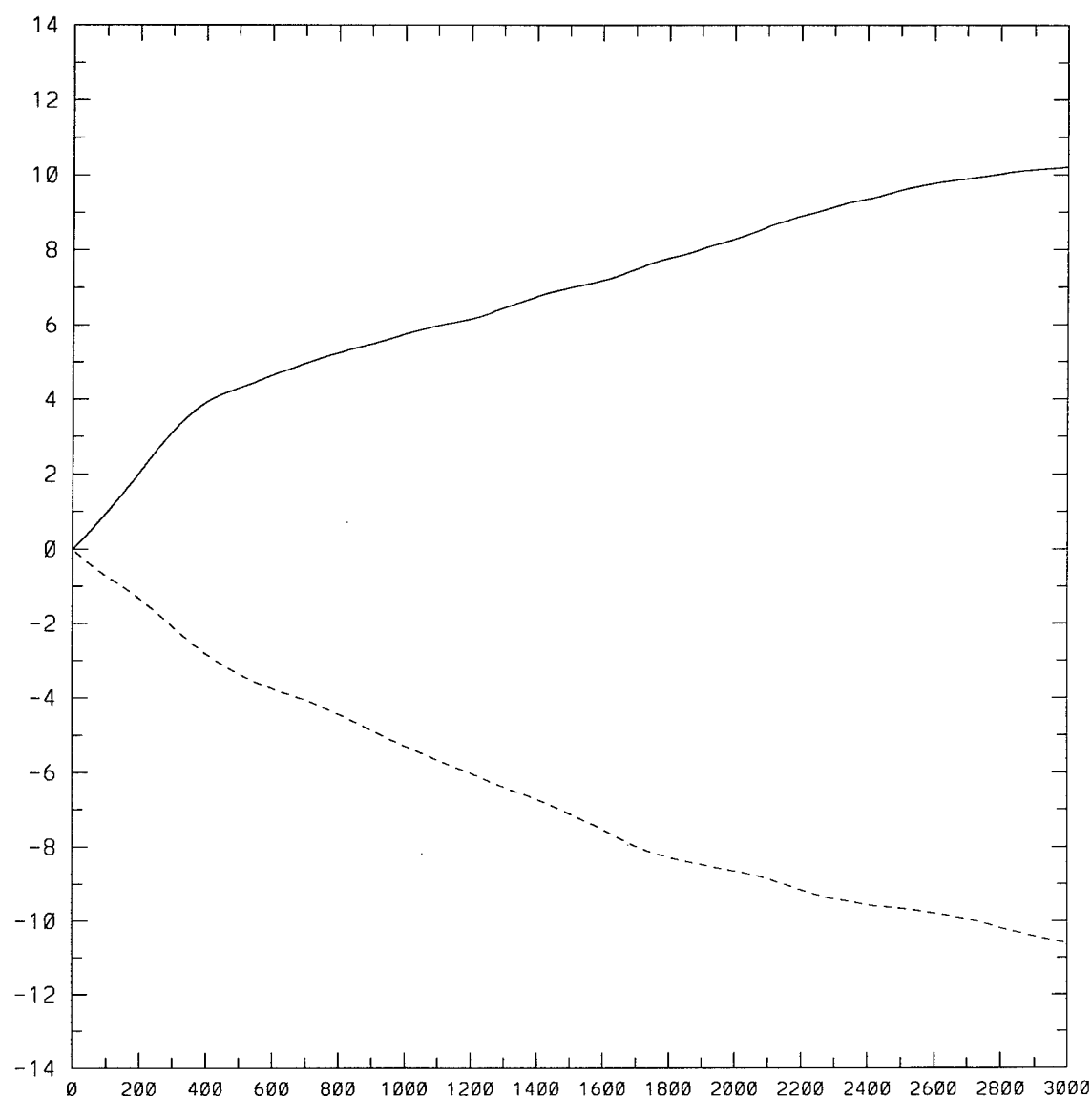


Figure 33 As in figure 31 but for $K_{co} = 10$.

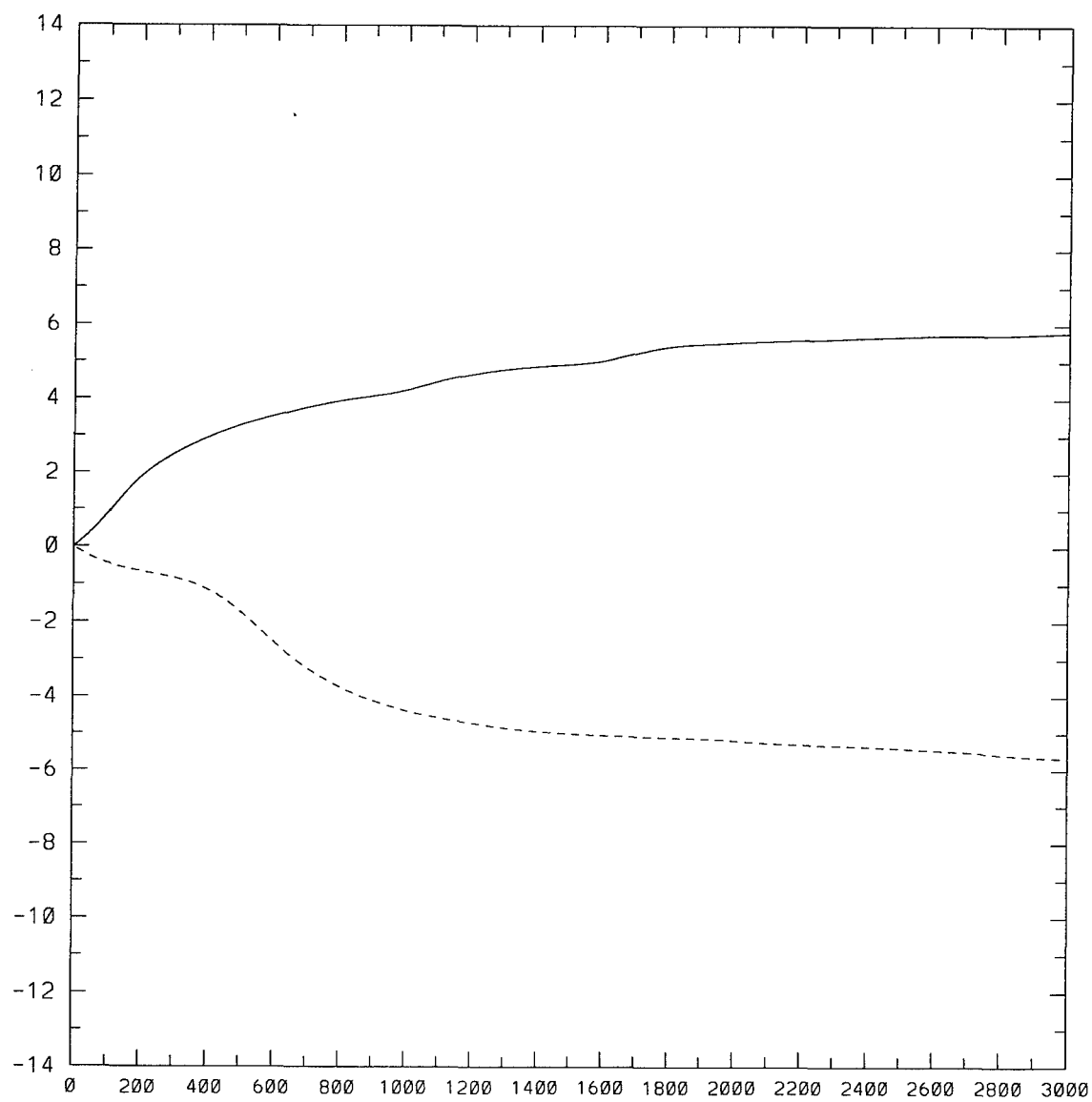


Figure 34 As in figure 31 but for $K_{co} = 5$.

The importance of small scale waves to tracer transport statistics is also seen in the velocity autocorrelation calculations for the four cases. Figure 35 shows the correlation of particles' zonal velocities (in the upper layer) with their initial conditions, thru 45 days of integration. As the previous figures in this section have shown, results for $K_{co}=5$ are dramatically different than for cases with higher cutoff wavenumbers. Velocities of particles in the low cutoff case are well correlated with initial conditions, indicating that the majority of particles spend their time in the easterlies. The other three curves in the figure show the zonal velocity autocorrelations for the $K_{co} \geq 10$ cases. The curves are very different, and in some instances, out of phase with each other (cutoff wavenumbers 60 and 20 at day 7, for example). Particle velocities for these wavenumbers rapidly decorrelate from initial conditions, with the full simulation decorrelating the fastest. In fact, for the case with all scales included ($K_{co}=60$), the average position of particles initialized in the easterlies is often in the westerlies. This situation never occurs with the $K_{co}=10$ or 5 simulations, and only occurs for the $K_{co}=20$ case after 30 days of integration. This suggest that the small scales play a key role in the mixing of particles.

Figure 36 shows the same statistic for the meridional velocities of the particles. Again, all of the curves are different, indicating that small scales play an important role in tracer transport. Unlike the zonal autocorrelations, the meridional velocity autocorrelation curves are centered around zero, and each zero crossing

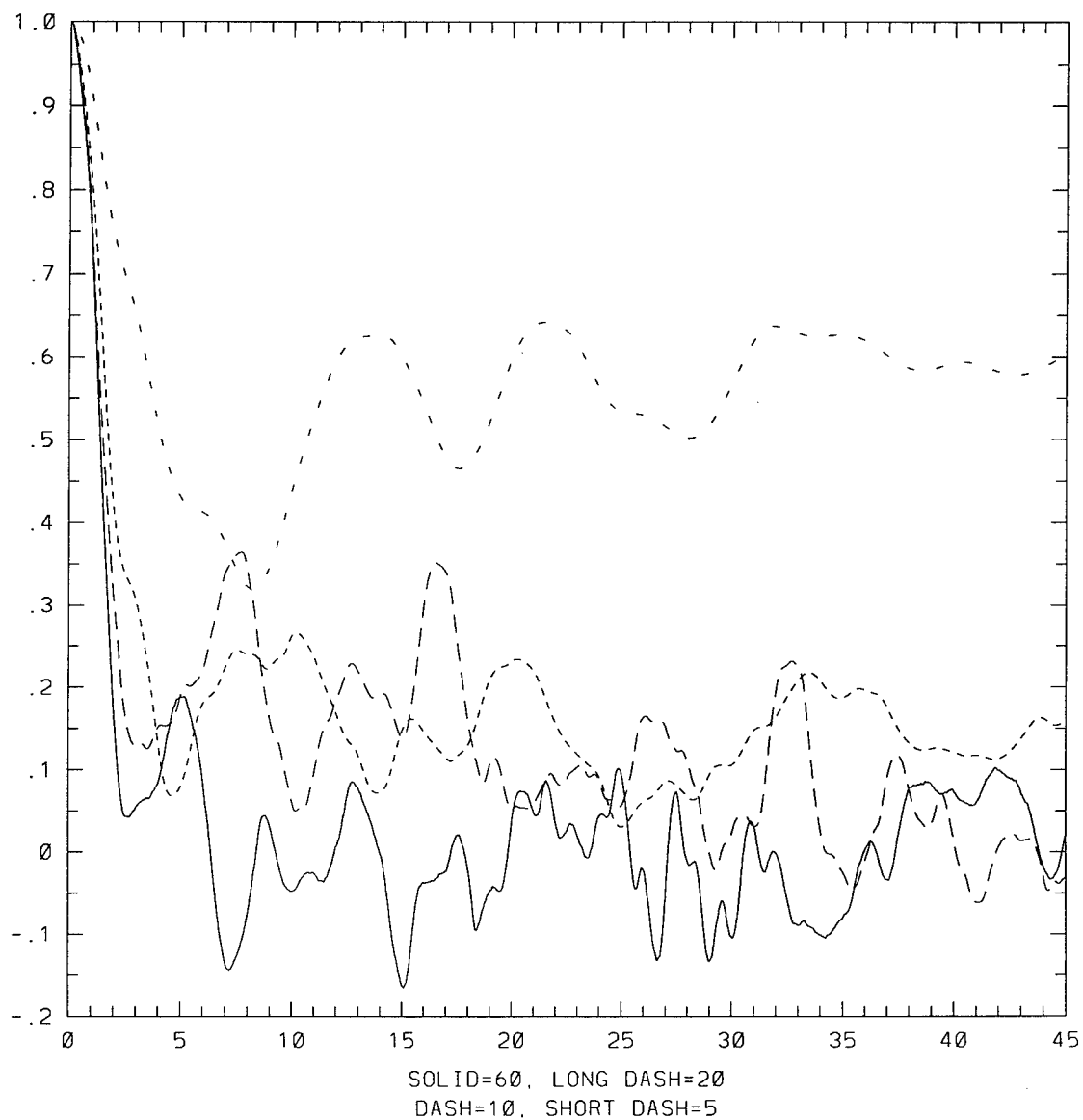


Figure 35 Zonal velocity autocorrelations for the four cases. Correlation coefficient on ordinate, nondimensional time on abscissa.

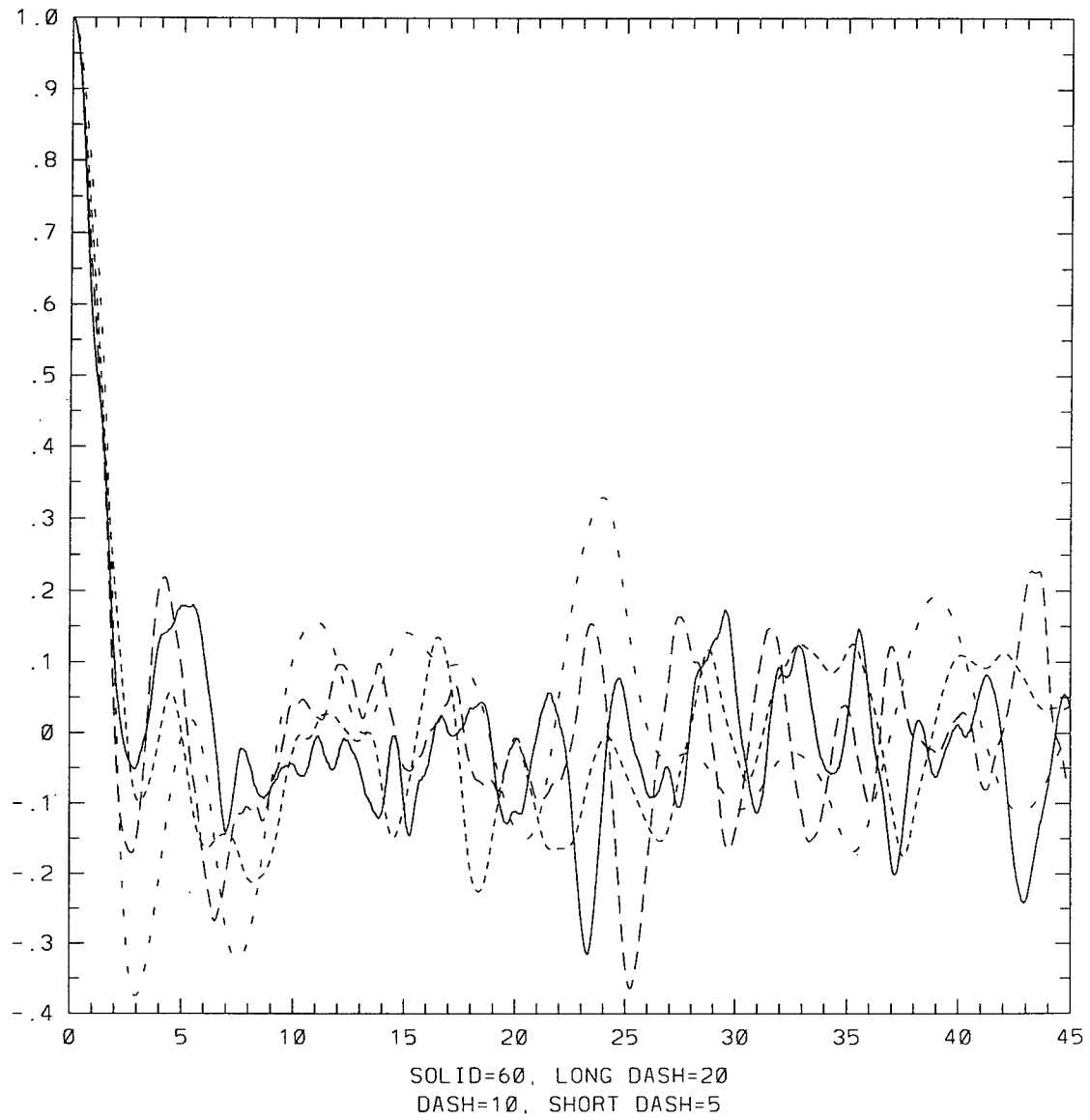


Figure 36 As in figure 35 but for meridional velocities.

reflects a reversal in the average direction of movement of particles compared to their initial conditions. Again, there are instances in the meridional flow, when the movement of particles in two cases is of opposite sign (cutoff wavenumbers 60 and 5 at days 7 and 12, for example).

Table 3 lists the Lagrangian integral timescales obtained from the autocorrelations coefficient curves for the 45 day integration period. Again, the results reflect the dependence of tracer statistics on cutoff wavenumber.

Thus, while Haidvogel (1985) claimed that only wavenumbers less than or equal to 10 needed to be included in the flow to accurately represent tracer transport statistics, results for scale sensitivity in the model used in this research indicate that for accuracy in some statistics, small scale effects must be included. A connection between Rossby wave-breaking and particle dispersion was made in the previous section of these results, and this relationship may explain the effect of scale selection on tracer transport in these four cases. Figure 37 is a time series (at half-day increments) of a portion of the upper-layer potential vorticity field for the full wavenumber simulation. There are three examples of wave-breaking in this segment of the domain. The large trough visible in the left side of the upper panel folds up on itself and releases a

Table 3 Lagrangian integral timescales for the scale sensitivity simulations.

$K_{co} =$	60	20	10	5
zonal	1.5	6.4	8.2	25.6
merid	.29	.64	.26	.93

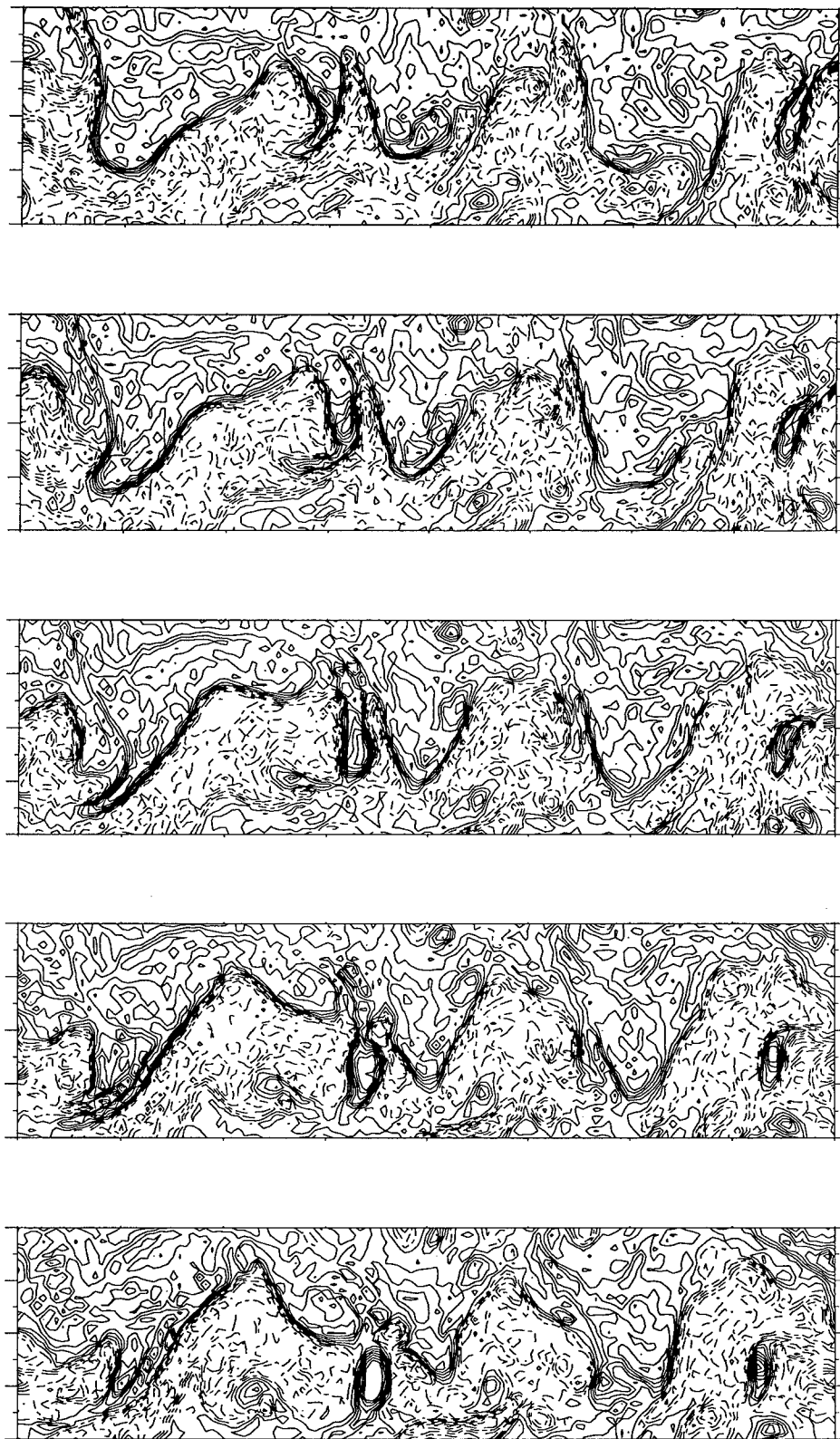


Figure 37 Wave-breaking time series for $K_{co} = 60$.

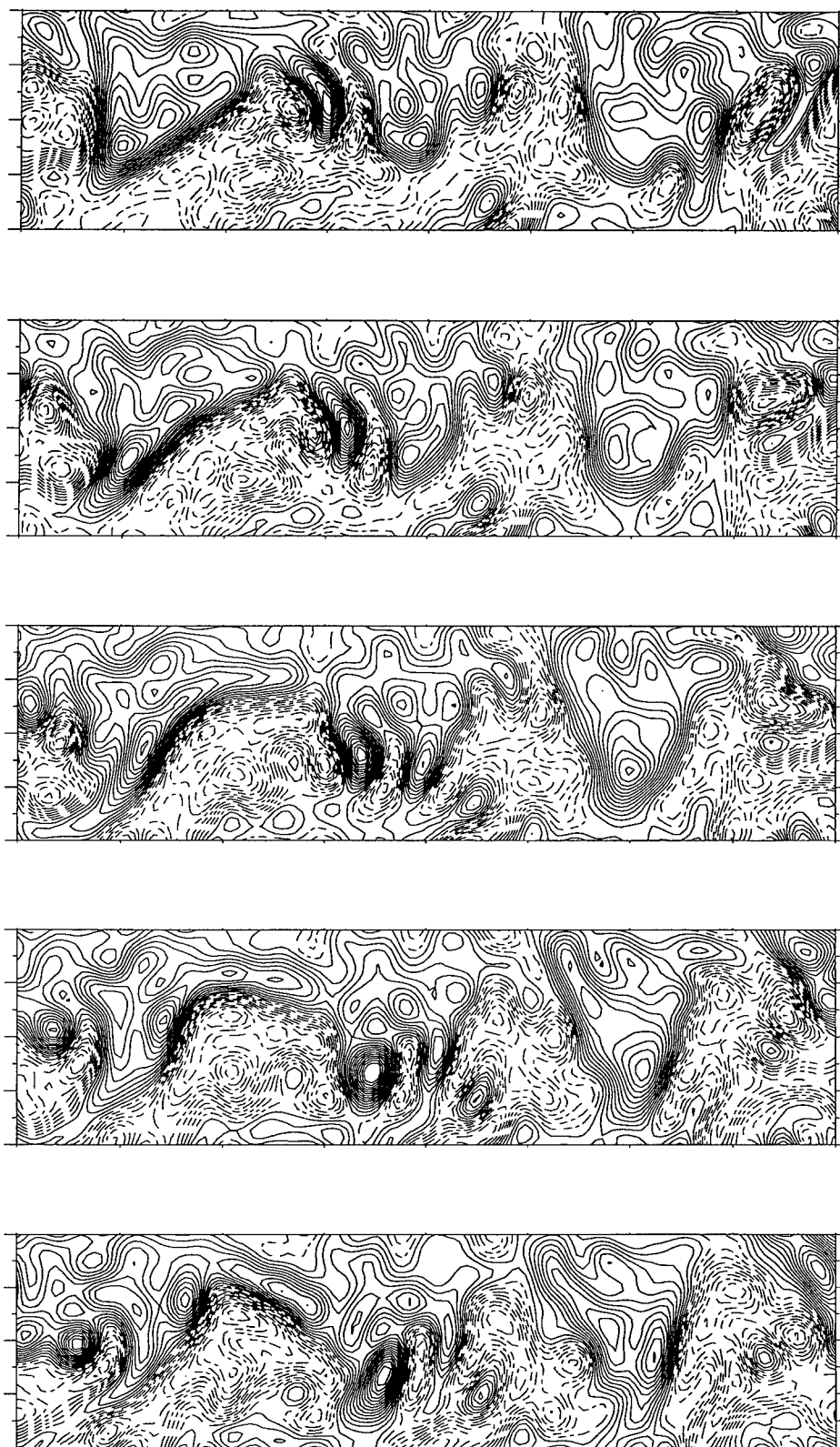


Figure 38 As in figure 37 but for $K_{co} = 20$.

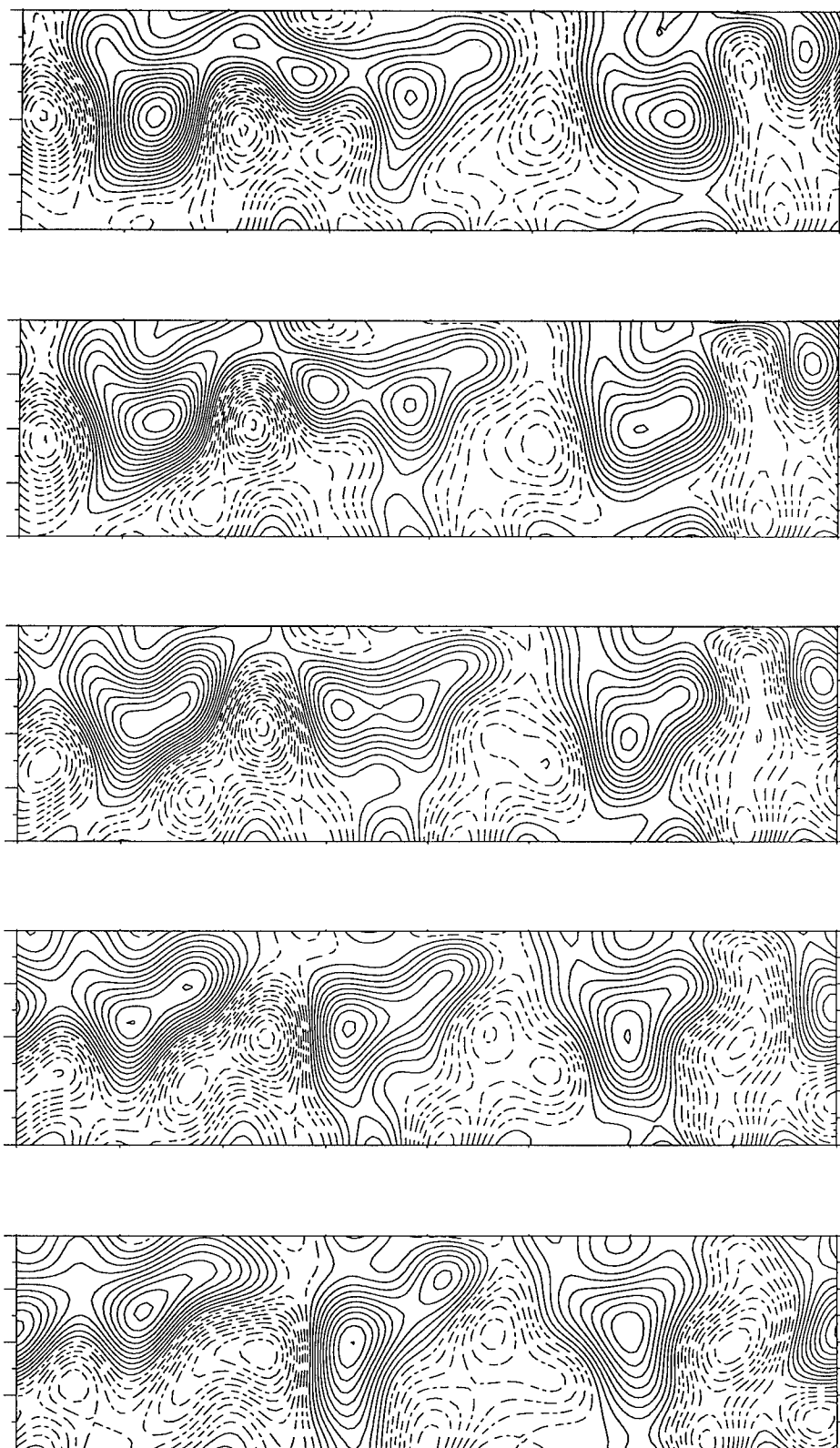


Figure 39 As in figure 37 but for $K_{co} = 10$.

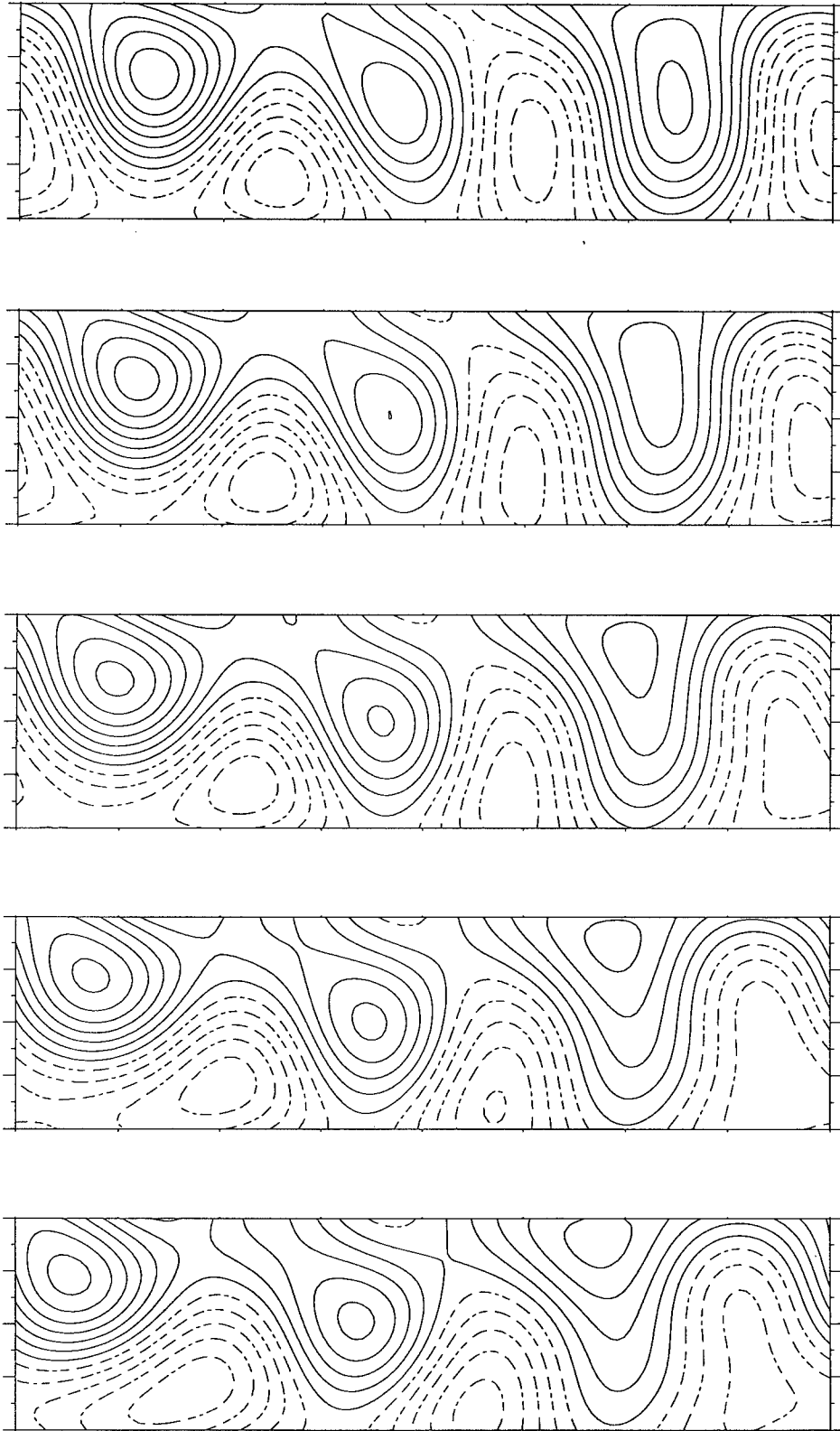


Figure 40 As in figure 37 but for $K_{co} = 5$.

filament of positive potential vorticity (solid lines) to the southwest. The “M” shaped feature to the left of center in the upper panel compresses and releases a vortex south of the jet. Finally, a wave on the right side of the upper panel has already collapsed, and is also ejecting a vortex into the flow south of the jet. Figure 38 is the same time series with wavenumbers larger than 20 removed. The three examples of wave-breaking are still clearly seen, but there is a noticeable “smoothing” of the potential vorticity contours. (Again, the contour interval in figure 37 is twice as large as the interval used in figures 38-40 for clarity.) Some features are lost entirely in the $K_{co}=20$ case, such as the filament released from the southern side of the forming vortex in the middle of the second panel (see full wavenumber case). As the cutoff wavenumber is further reduced, the wave-breaking is reduced. Figure 39 shows the time series for the $K_{co}=10$ case. Here, the vortex on the right side of the panels never forms, eliminating one method of transporting tracers southward across the jet. Similarly, no clear filament is formed from the breaking wave on the left side of the panels, further reducing the means for meridional dispersion. The middle vortex evident in the full wavenumber case also never forms in the $K_{co}=10$ case, although the potential vorticity gradient in that region does orient itself in a north/south direction, allowing meridional transport of any tracers on either side of the gradient. Finally, figure 40 shows the time series for the $K_{co}=5$ case. In these panels, there are no filaments or vortices formed, and wave-breaking takes on the form of regions of positive or

negative potential vorticity becoming disconnected from each other. The center of the bottom panel shows a wave reforming, i.e., two regions of positive p.v. are being reconnected. There is certainly no "crashing" of waves with subsequent ejection of material, however.

It seems, then, that the importance of a particular wavenumber to tracer transport may depend upon the wavenumber's contribution to Rossby wave-breaking along the maximum potential vorticity gradient at the westerly jet core. Including only the large waves in the flow eliminates much of the breaking and results in decreased meridional dispersions. It is also not clear that including only the large waves gives accurate results for tracer statistics. It appears, then, that the model used in this research is sensitive to the scale of waves included in the flow.

CHAPTER V

SUMMARY AND CONCLUSIONS

This research characterizes tracer dispersion in a system that combines the efficiency of turbulent mixing, the anisotropy of zonal jets, and the unpredictability of Rossby wave-breaking events.

Results of simulations with two different values of the planetary vorticity gradient showed the need to develop a new time- and lengthscale to enable comparison of the disparate regimes. An Eulerian timescale was devised, based upon the values of the eddy kinetic energy and weighted eddy kinetic energy of the flow. The new lengthscale took into account the difference in average distance from easterly to westerly jet cores in the two beta cases. Analysis of tracer dispersion statistics and trajectories using these new scales indicates that an increase in beta results in increased zonal transport, while meridional transport away from the westerly jet core is comparable in the two cases. Increasing β also results in a increase in particle spreading. Similarly, since the energy of the flow decreases as β is increased, Rossby wave-breaking is diminished in the high-beta case, resulting in diminished tracer transport across jets.

The scale sensitivity experiments confirm that wave-breaking plays a key role in tracer dispersion. As the number of waves removed from the flow increases, the maximum potential vorticity gradient associated with the jet core is smoothed

and small-scale features of the flow, such as filaments and vortices, no longer appear. Wave-breaking diminishes and the jets become less permeable. As a result, zonal single-particle displacements are enhanced and meridional rms displacements decrease. Zonal velocities of particles remain correlated with initial conditions much longer when small scales are removed, and on average, the zonal and meridional Lagrangian integral time scales increase as the cutoff wavenumber decreases. The removal of small scales also has an effect on the two-particle statistics, and results in an increase in particle spreading as waves are truncated from the flow. Thus, the scale sensitivity simulations confirm that, for systems where enstrophy is dissipated by hyperviscosity, all scales of waves must be included in the flow in order to accurately characterize tracer dispersion.

REFERENCES

- Bowman, K. P., 1993: Large-scale isentropic mixing properties of the Antarctic polar vortex from analyzed winds. *J. Geophys. Res.*, **98**, 23013-23027.
- , 1995: Diffusive transport by breaking waves. *J. Atmos. Sci.*, **52**, 2416-2427.
- , and P. Chen, 1994: Mixing by barotropic instability in a nonlinear model. *J. Atmos. Sci.*, **51**, 3692-3705.
- Ellis, W. G., and J. T. Merrill, 1995: Trajectories for Saharan dust transported to Barbados using Stoke's Law to describe gravitational settling. *J. Appl. Meteor.*, **34**, 1716-1726.
- Haidvogel, D. B., 1982: On the feasibility of particle tracking in Eulerian ocean models. *Ocean Modelling*, **45**, 4-9.
- , 1985: Particle dispersion and Lagrangian vorticity conservation in models of β -plane turbulence. (Unpublished manuscript). Personal collection, Jennifer Roman.
- Holton, J. R., 1992: *An Introduction to Dynamic Meteorology*, Academic Press, Inc., 511 pp.
- Hua, B. L., 1994: The conservation of potential vorticity along Lagrangian trajectories in simulations of eddy-driven flows. *J. Phys. Oceanogr.*, **24**, 498-508.
- Huang, M. J., and A. Leonard, 1995: Velocity autocorrelations of decaying isotropic homogeneous turbulence. *Phys. Fluids*, **7**, 2455-2464.
- Juckes, M. N., and M. E. McIntyre, 1985: A high-resolution one-layer model of breaking planetary waves in the stratosphere. *Nature*, **328**, 590-596.
- McIntyre, M. E., and T. N. Palmer, 1983: Breaking planetary waves in the stratosphere. *Nature*, **305**, 593-600.
- Nakamura, M., and R. A. Plumb, 1994: The effects of flow asymmetry on the direction of Rossby wave breaking. *J. Atmos. Sci.*, **51**, 2031-2045.
- Orszag, S. A., 1971: Numerical simulation of incompressible flows within simple boundaries. I. Galerkin (spectral) representations. *Stud. Appl. Math.*, **50**, 293-327.

- Panetta, R. L., 1993: Zonal jets in wide baroclinically unstable regions: persistence and scale selection. *J. Atmos. Sci.*, **50**, 2073-2106.
- Pedlosky J., 1987: *Geophysical Fluid Dynamics*. 2d ed. Springer- Verlag, 710 pp.
- Pierrehumbert, R. T., 1991a: Large-scale horizontal mixing in planetary atmospheres. *Phys. Fluids A*, **3**, 1250-1260.
- , 1991b: Chaotic mixing of tracer and vorticity by modulated travelling Rossby waves. *Geophys. Astrophys. Fluid Dynamics*, **58**, 285-319.
- Polvani, L. M., and R. A. Plumb, 1992: Rossby wave breaking, microbreaking, filamentation, and secondary vortex formation: The dynamics of a perturbed vortex. *J. Atmos. Sci.*, **49**, 462-476.
- Riley, J. J., and G. S. Patterson, 1975: Diffusion experiments with numerically integrated isotropic turbulence. *Phys. Fluids*, **17**, 292-297.
- Sommeria, J., Meyers, S. D., and H. L. Swinney, 1989: Laboratory model of a planetary eastward jet. *Nature*, **337**, 58-61.
- Taylor, G. I., 1921: Diffusion by continuous movements. *Proc. London Math. Soc. Ser. 2*, **20**, 196-212.
- Tennekes, H., and J. L. Lumley, 1972: *A First Course in Turbulence*. MIT Press, 300 pp.
- Yeung, P. K., and S. B. Pope, 1989: Lagrangian statistics from direct numerical simulations of isotropic turbulence. *J. Fluid Mech.*, **207**, 531-586.

APPENDIX

The dimensional evolution equations for potential vorticity are

$$\partial Q_1^*/\partial t^* + J(\Psi_1^*, Q_1^*) = -\nu^* \nabla^{10} \Psi_1^* \quad (1)$$

$$\partial Q_2^*/\partial t^* + J(\Psi_2^*, Q_2^*) = -\kappa_M^* \nabla^2 \Psi_2^* - \nu^* \nabla^{10} \Psi_2^*. \quad (2)$$

Working with the left hand side of equation (1)

$$\begin{aligned} \partial Q_1^*/\partial t^* + J(\Psi_1^*, Q_1^*) &= \frac{\partial}{\partial t^*} (\nabla^2 \Psi_1^* - \hat{\Psi}^*/\lambda^2) + \\ &(\partial \Psi_1^*/\partial x^*)(\partial Q_1^*/\partial y^*) - (\partial \Psi_1^*/\partial y^*)(\partial Q_1^*/\partial x^*) \end{aligned} \quad (1a)$$

$$\begin{aligned} &= \partial q_1^*/\partial t^* + \partial \psi_1^*/\partial x^* (\beta^* + \frac{\partial}{\partial y^*} (\nabla^2 \Psi_1^* - \hat{\Psi}^*/\lambda^2)) - \\ &(\partial \psi_1^*/\partial y^* - U_0) \frac{\partial}{\partial x^*} (\nabla^2 \Psi_1^* - \hat{\Psi}^*/\lambda^2) \end{aligned} \quad (1b)$$

$$\begin{aligned} &= \partial q_1^*/\partial t^* + \beta^* \partial \psi_1^*/\partial x^* + (\partial \psi_1^*/\partial x^*) \frac{\partial}{\partial y^*} (\nabla^2 \Psi_1^*) - (\partial \psi_1^*/\partial x^*) (1/2\lambda^2) \frac{\partial}{\partial y^*} (\psi_1^* - \\ &U_0 y^* - \psi_2^*) - (\partial \psi_1^*/\partial y^*) \frac{\partial}{\partial x^*} (\nabla^2 \Psi_1^*) + (\partial \psi_1^*/\partial y^*) (1/2\lambda^2) \frac{\partial}{\partial x^*} (\psi_1^* - \\ &U_0 y^* - \psi_2^*) + U_0 \frac{\partial}{\partial x^*} (\nabla^2 \Psi_1^*) - U_0 (1/2\lambda^2) \frac{\partial}{\partial x^*} (\psi_1^* - U_0 y^* - \psi_2^*) \end{aligned} \quad (1c)$$

$$\begin{aligned} &= \partial q_1^*/\partial t^* + \beta^* \partial \psi_1^*/\partial x^* + (\partial \psi_1^*/\partial x^*) \frac{\partial}{\partial y^*} (\nabla^2 \psi_1^*) - (\partial \psi_1^*/\partial x^*) \frac{\partial}{\partial y^*} (\hat{\psi}^*/\lambda^2) + \\ &(\partial \psi_1^*/\partial x^*) (U_0/2\lambda^2) - (\partial \psi_1^*/\partial y^*) \frac{\partial}{\partial x^*} (\nabla^2 \psi_1^*) + (\partial \psi_1^*/\partial y^*) \frac{\partial}{\partial x^*} (\hat{\psi}^*/\lambda^2) + \\ &U_0 \frac{\partial}{\partial x^*} (\nabla^2 \psi_1^*) - U_0 \frac{\partial}{\partial x^*} (\hat{\psi}^*/\lambda^2) \end{aligned} \quad (1d)$$

$$\begin{aligned} &= \partial q_1^*/\partial t^* + (\partial \psi_1^*/\partial x^*) \frac{\partial}{\partial y^*} (\nabla^2 \psi_1^* - \hat{\psi}^*/\lambda^2) - (\partial \psi_1^*/\partial y^*) \frac{\partial}{\partial x^*} (\nabla^2 \psi_1^* - \\ &\hat{\psi}^*/\lambda^2) + (\partial \psi_1^*/\partial x^*) (\beta^* + U_0/2\lambda^2) + U_0 (\partial q_1^*/\partial x^*) \end{aligned} \quad (1e)$$

So,

$$\partial q_1^*/\partial t^* + J(\psi_1^*, q_1^*) + (\partial \psi_1^*/\partial x^*)(\beta^* + U_0/2\lambda^2) + U_0(\partial q_1^*/\partial x^*) = RHS \quad (1f)$$

Or,

$$\begin{aligned} \partial q_1^*/\partial t^* + J(\psi_1^*, q_1^*) = \\ -U_0(\partial q_1^*/\partial x^*) - (\partial \psi_1^*/\partial x^*)(\beta^* + U_0/2\lambda^2) - \nu^* \nabla^{10} \psi_1^* \end{aligned} \quad (3)$$

Working with the left hand side of equation (2)

$$\begin{aligned} \partial Q_2^*/\partial t^* + J(\Psi_2^*, Q_2^*) = \frac{\partial}{\partial t^*}(\nabla^2 \Psi_2^* - \hat{\Psi}^*/\lambda^2) + \\ (\partial \Psi_2^*/\partial x^*)(\partial Q_2^*/\partial y^*) - (\partial \Psi_2^*/\partial y^*)(\partial Q_2^*/\partial x^*) \end{aligned} \quad (2a)$$

$$\begin{aligned} = \partial q_2^*/\partial t^* + \partial \psi_2^*/\partial x^*(\beta^* + \frac{\partial}{\partial y^*}(\nabla^2 \Psi_2^* - \hat{\Psi}^*/\lambda^2)) - \\ (\partial \psi_2^*/\partial y^*) \frac{\partial}{\partial x^*}(\nabla^2 \Psi_2^* - \hat{\Psi}^*/\lambda^2) \end{aligned} \quad (2b)$$

$$\begin{aligned} = \partial q_2^*/\partial t^* + \beta^* \partial \psi_2^*/\partial x^* + (\partial \psi_2^*/\partial x^*) \frac{\partial}{\partial y^*}(\nabla^2 \Psi_2^*) + (\partial \psi_2^*/\partial x^*)(1/2\lambda^2) \frac{\partial}{\partial y^*}(\psi_1^* - \\ U_0 y^* - \psi_2^*) - (\partial \psi_2^*/\partial y^*) \frac{\partial}{\partial x^*}(\nabla^2 \Psi_2^*) - (\partial \psi_2^*/\partial y^*)(1/2\lambda^2) \frac{\partial}{\partial x^*}(\psi_1^* - \\ U_0 y^* - \psi_2^*) \end{aligned} \quad (2c)$$

$$\begin{aligned} = \partial q_2^*/\partial t^* + \beta^* \partial \psi_2^*/\partial x^* + (\partial \psi_2^*/\partial x^*) \frac{\partial}{\partial y^*}(\nabla^2 \psi_2^*) + (\partial \psi_2^*/\partial x^*) \frac{\partial}{\partial y^*}(\hat{\psi}^*/\lambda^2) - \\ (\partial \psi_2^*/\partial x^*)(U_0/2\lambda^2) - (\partial \psi_2^*/\partial y^*) \frac{\partial}{\partial x^*}(\nabla^2 \psi_2^*) - (\partial \psi_2^*/\partial y^*) \frac{\partial}{\partial x^*}(\hat{\psi}^*/\lambda^2) \end{aligned} \quad (2d)$$

$$\begin{aligned} = \partial q_2^*/\partial t^* + (\partial \psi_2^*/\partial x^*) \frac{\partial}{\partial y^*}(\nabla^2 \psi_2^* + \hat{\psi}^*/\lambda^2) - (\partial \psi_2^*/\partial y^*) \frac{\partial}{\partial x^*}(\nabla^2 \psi_2^* + \\ \hat{\psi}^*/\lambda^2) + (\partial \psi_2^*/\partial x^*)(\beta^* - U_0/2\lambda^2) \end{aligned} \quad (2e)$$

So,

$$\partial q_2^*/\partial t^* + J(\psi_2^*, q_2^*) + (\partial \psi_2^*/\partial x^*)(\beta^* - U_0/2\lambda^2) = RHS \quad (2f)$$

Or,

$$\begin{aligned} \partial q_2^*/\partial t^* + J(\psi_2^*, q_2^*) = \\ -(\partial \psi_2^*/\partial x^*)(\beta^* - U_0/2\lambda^2) - \kappa_M^* \nabla^2 \psi_2^* - \nu^* \nabla^{10} \psi_2^* \end{aligned} \quad (4)$$

Thus, the dimensional equations may also be written as

$$\begin{aligned} \partial q_1^*/\partial t^* + J(\psi_1^*, q_1^*) = \\ -U_0(\partial q_1^*/\partial x^*) - (\partial \psi_1^*/\partial x^*)(\beta^* + U_0/2\lambda^2) - \nu^* \nabla^{10} \psi_1^* \end{aligned} \quad (3)$$

$$\begin{aligned} \partial q_2^*/\partial t^* + J(\psi_2^*, q_2^*) = \\ -(\partial \psi_2^*/\partial x^*)(\beta^* - U_0/2\lambda^2) - \kappa_M^* \nabla^2 \psi_2^* - \nu^* \nabla^{10} \psi_2^*. \end{aligned} \quad (4)$$

Using the following nondimensionalization parameters

$$Q_i^* = Q_i U_0 / \lambda, \quad \Psi_i^* = \Psi_i \lambda U_0, \quad \nu^* = \nu U_0 \lambda^7$$

$$\beta^* = \beta U_0 / \lambda^2, \quad \kappa_M^* = \kappa_M U_0 / \lambda,$$

equation (3) may be written as (with boxes indicating dimensions)

$$\begin{aligned} \left[\frac{U_o/\lambda}{\lambda/U_o} \right] \partial q_1 / \partial t + \left[\frac{\lambda U_o}{\lambda} \frac{U_o/\lambda}{\lambda} \right] J(\psi_1, q_1) = - \left[\frac{U_o}{\lambda} \frac{U_o/\lambda}{\lambda} \right] (\partial q_1 / \partial x) - \\ \left[\frac{U_o}{\lambda^2} \right] (\beta + \frac{1}{2}) \left[\frac{U_o \lambda}{\lambda} \right] (\partial \psi_1 / \partial x) - \left[U_o \lambda^7 \right] \nu \left[\frac{U_o \lambda}{\lambda^{10}} \right] \nabla^{10} \psi_1 \end{aligned} \quad (3b)$$

$$\begin{aligned} \left[\frac{U_o^2}{\lambda^2} \right] \partial q_1 / \partial t + \left[\frac{U_o^2}{\lambda^2} \right] J(\psi_1, q_1) = - \left[\frac{U_o^2}{\lambda^2} \right] (\partial q_1 / \partial x) - \\ \left[\frac{U_o^2}{\lambda^2} \right] (\beta + \frac{1}{2}) (\partial \psi_1 / \partial x) - \left[\frac{U_o^2}{\lambda^2} \right] \nu \nabla^{10} \psi_1 \end{aligned} \quad (3c)$$

and equation (4) may be written as (with boxes indicating dimensions)

$$\begin{aligned} \left[\frac{U_o/\lambda}{\lambda/U_o} \right] \partial q_2 / \partial t + \left[\frac{\lambda U_o}{\lambda} \frac{U_o/\lambda}{\lambda} \right] J(\psi_2, q_2) = - \left[\frac{U_o}{\lambda^2} \right] (\beta - \tfrac{1}{2}) \left[\frac{U_o \lambda}{\lambda} \right] (\partial \psi_2 / \partial x) - \\ \left[\frac{U_o}{\lambda} \right] \kappa_M \left[\frac{U_o \lambda}{\lambda^2} \right] \nabla^2 \psi_2 - \left[U_0 \lambda^7 \right] \nu \left[\frac{U_o \lambda}{\lambda^{10}} \right] \nabla^{10} \psi_2 \end{aligned} \quad (4b)$$

$$\begin{aligned} \left[\frac{U_o^2}{\lambda^2} \right] \partial q_2 / \partial t + \left[\frac{U_o^2}{\lambda^2} \right] J(\psi_2, q_2) = - \left[\frac{U_o^2}{\lambda^2} \right] (\beta - \tfrac{1}{2}) (\partial \psi_2 / \partial x) - \\ \left[\frac{U_o^2}{\lambda^2} \right] \kappa_M \nabla^2 \psi_2 - \left[\frac{U_o^2}{\lambda^2} \right] \nu \nabla^{10} \psi_2 \end{aligned} \quad (4c)$$

Dividing (3c) and (4c) by $\frac{U_o^2}{\lambda^2}$ gives the nondimensional equations:

$$\partial q_1 / \partial t + J(\psi_1, q_1) = -\partial q_1 / \partial x - (\beta + \tfrac{1}{2}) \partial \psi_1 / \partial x - \nu \nabla^{10} \psi_1 \quad (5)$$

$$\partial q_2 / \partial t + J(\psi_2, q_2) = -(\beta + \tfrac{1}{2}) \partial \psi_2 / \partial x - \kappa_M \nabla^2 \psi_2 - \nu \nabla^{10} \psi_2 \quad (6)$$

VITA

Jennifer Claire Roman [REDACTED], on 5 May 1970 to Col. (Ret.) Edward and Mary Alexander. An Army brat, she grew up in four overseas and three stateside locations. She graduated from Allied Forces Central Europe (AFCENT) International High School in the Netherlands in 1988, and entered the University of Arizona with a four-year Air Force ROTC Scholarship. She graduated Magna Cum Laude in May 1992 with a B.S. in Atmospheric Sciences, and was commissioned in the United States Air Force. Five months later, Lieutenant Roman was assigned to the 410th Bomb Wing at K.I. Sawyer Air Force Base, Gwinn, Michigan. As Wing Weather Officer, Lt. Roman provided support to the B-52H, KC-135 and T-37 aircraft on station, as well as over a dozen reserve and guard units throughout the Upper Midwest. Lt. Roman was accepted to the AFIT program in 1994, and was reassigned to Texas A&M University in August of that year.

Lieutenant Roman may be reached through her parents, [REDACTED]
[REDACTED]